

1 Substantially positive contributions of new particle formation to Cloud Condensation
2 Nuclei under low supersaturation in China based on numerical model improvements

3

4 Chupeng Zhang^{1#}, Shangfei Hai^{2,12#}, Yang Gao^{1*}, Yuhang Wang^{3*}, Shaoqing Zhang^{4,2},
5 Lifang Sheng², Bin Zhao⁵, Shuxiao Wang⁵, Jingkun Jiang⁵, Xin Huang⁶, Shen Xiaojing⁷,
6 Sun Junying⁷, Aura Lupascu^{8,9}, Manish Shrivastava¹⁰, Jerome D. Fast¹⁰, Wenxuan
7 Cheng¹, Xiuwen Guo¹, Ming Chu¹, Nan Ma¹¹, Juan Hong¹¹, Qiaoqiao Wang¹⁰,
8 Xiaohong Yao¹ and Huiwang Gao¹

9

10 ¹Frontiers Science Center for Deep Ocean Multispheres and Earth System, and Key Laboratory of
11 Marine Environmental Science and Ecology, Ministry of Education, Ocean University of China,
12 and Laoshan Laboratory, Qingdao, 266100, China

13 ²College of Oceanic and Atmospheric Sciences, Ocean University of China, Qingdao, 266100,
14 China

15 ³School of Earth and Atmospheric Sciences, Georgia Institute of Technology, Atlanta, GA, 30332,
16 USA

17 ⁴Frontiers Science Center for Deep Ocean Multispheres and Earth System, and Key Laboratory of
18 Physical Oceanography, Ocean University of China, and Laoshan Laboratory, Qingdao, 266100,
19 China

20 ⁵State Key Joint Laboratory of Environment Simulation and Pollution Control, School of
21 Environment, Tsinghua University, Beijing, 100084 China, and State Environmental Protection
22 Key Laboratory of Sources and Control of Air Pollution Complex, Beijing 100084, China

23 ⁶School of Atmospheric Sciences, Nanjing University, Nanjing, 210023, China

24 ⁷State Key Laboratory of Severe Weather & Key Laboratory of Atmospheric Chemistry of CMA,
25 Chinese Academy of Meteorological Sciences, Beijing, 100081, China

26 ⁸Institute for Advanced Sustainability Studies, Potsdam D-14467, Germany

27 ⁹ECMWF, Bonn, 53111, Germany

28 ¹⁰Atmospheric Sciences and Global Change Division, Pacific Northwest National Laboratory,
29 Richland, WA, 99354, USA

30 ¹¹Institute for Environmental and Climate Research, Jinan University, Guangzhou, 510000, China

31 ¹²CMA Earth System Modeling and Prediction Center, China Meteorological Administration,
32 Beijing 100081, China

33

#Authors contributed equally to this study.

34

*To whom correspondence to: yanggao@ouc.edu.cn, yuhang.wang@eas.gatech.edu

35

36

37

Abstract

38 New particle formation (NPF) and subsequent particle growth are important sources of
39 condensation nuclei (CN) and cloud condensation nuclei (CCN). While many
40 observations have shown positive contributions of NPF to CCN at low supersaturation,
41 negative NPF contributions were often simulated in polluted environments. Using the
42 observations in a coastal city of Qingdao, Beijing and Gucheng in North China, we
43 thoroughly evaluate the simulated number concentrations of CN and CCN using a NPF-
44 explicit parameterization embedded in WRF-Chem model. For CN, the initial
45 simulation shows large biases of particle number concentrations at 10–40 nm and 40–
46 100 nm. By adjusting the process of gas-particle partitioning, including the mass
47 accommodation coefficient of sulfuric acid, the phase changes of primary organic
48 aerosol emissions and the condensational amount of nitric acid, the improvement of the
49 particle growth process yields a substantially reduced overestimates of CN. Regarding
50 CCN, SOA formed from the oxidation of semi-volatile and intermediate volatility
51 organic vapors (SI-SOA) yield is an important contributor. At default settings, the SI-
52 SOA yield is too high without considering the differences in precursor oxidation rates.
53 Lowering the SI-SOA yield under linear-H₂SO₄ nucleation scheme results in much
54 improved CCN simulations compared to observations. On the basis of the bias-
55 corrected model, we find substantially positive contributions of NPF to CCN at low
56 supersaturation (~0.2%) over the broad areas of China, primarily due to competing
57 effects of increasing particle hygroscopicity, a result of reductions in SI-SOA amount,
58 surpassing that of particle size decreases. The bias-corrected model is robustly
59 applicable to other schemes, such as quadratic-H₂SO₄ nucleation scheme, in terms of
60 CN and CCN, though the dependence of CCN on SI-SOA yield is diminished likely
61 due to changes in particle composition. This study highlights the potentially much
62 larger NPF contributions to CCN on a regional and even global basis.

63

64

65

66

67 **1. Introduction**

68 New particle formation (NPF) is a process in which gaseous vapors nucleate and
69 form critical molecular clusters, followed by subsequent growth to larger sizes through
70 condensation and coagulation (Kulmala et al., 2004; Kulmala et al., 2013; Lee et al.,
71 2019). Newly formed particles could effectively grow into the size of cloud
72 condensation nuclei (CCN) under certain supersaturation (SS), which exerts an impact
73 on the cloud microphysical process and global radiation balance (Merikanto et al., 2007;
74 Kerminen et al., 2018; Ren et al., 2021). In addition, the efficient nucleation and
75 explosive growth of particles may contribute to the formation of haze (Guo et al., 2014),
76 affecting air quality and human health (Yuan et al., 2015; Chu et al., 2019; Kulmala et
77 al., 2021).

78 The overestimate of condensation nuclei (CN) in numerical models is commonly
79 seen, despite the attempt to rectify the bias (Matsui et al., 2013; Arghavani et al., 2022).
80 It is a common way to reduce the nucleation rate which may reduce the particle number
81 concentration in proportion (Matsui et al., 2013). For instance, in the study of NPF in
82 East Asia in the spring of 2009, even after lowering the nucleation rate in a regional
83 model of WRF-Chem applied in their study, the reduced number concentration of
84 particles at 10–130 nm remained to be overestimated (Matsui et al., 2013). Using the
85 same regional model and a similar method to reduce the nucleation rate, Arghavani et
86 al. (2022) found particle number concentration at 10–100 nm was still overestimated
87 by nearly one order of magnitude, despite the effectiveness to reduce the overestimates
88 for the smaller particles such as 2.5–10 nm. In addition to the rate of NPF, the growth
89 process of particles also has a crucial effect on particle number concentration and size
90 distribution. In this process, the condensation of some chemical species such as sulfuric
91 acid, nitrate and organic gases on particles plays a major role in particle growth (Yao et
92 al., 2018; Lee et al., 2019; Li et al., 2022), and the uncertainty of their condensation
93 amount may lead to the bias of CN simulation.

94 In addition to CN, there are large discrepancies in the predicted CCN between the
95 numerical models and observational results. Furthermore, as an important source of

96 CCN (Merikanto et al., 2009), the contribution of nucleation to CCN quantified by
97 numerical models is also highly uncertain. For example, in terms of predicting CCN,
98 Fanourgakis et al. (2019) evaluated the CCN concentrations simulated by 16 global
99 aerosol–climate and chemistry transport models with observations at 9 sites in Europe
100 and Japan from 2011 to 2015, and found that all models underestimated CCN
101 concentrations with a mean normalized mean bias of -36% at low supersaturation
102 ($SS=0.2\%$). WRF-Chem models also tend to underestimate the contribution of NPF to
103 CCN, especially at low supersaturation. The continuous observation of CCN
104 concentrations throughout the year (July 2008–June 2009) carried out in Hyytiälä,
105 Finland, showed that under low SS, nucleation enhanced the CCN by 106% and 110%
106 at $SS=0.1\%$ and 0.2% respectively (Sihto et al., 2011). Observations acquired in Beijing
107 from July 12 to September 25, 2008, also suggested that nucleation significantly
108 increases CCN at all supersaturations, even when supersaturation is low (i.e., 0.07%
109 and 0.26%). Thus, the occurrence of NPF enhanced CCN by a factor of 1.7 and 2.2,
110 respectively (Yue et al., 2011).

111 However, previous numerical experiments behave oppositely. For instance, Matsui
112 et al. (2011) quantified the contribution of nucleation to CCN using WRF-chem in
113 Beijing in August and September 2006 and found reduced CCN under low SS, e.g.,
114 when $SS=0.02\%$, the concentration of CCN is reduced by up to $\sim 50\%$. They attributed
115 this to the fact that the small particles produced by nucleation may inhibit the growth
116 of the pre-existing particles (Matsui et al., 2011). Similarly, Dong et al. (2019)
117 conducted NPF simulations with the WRF-Chem for the summer of 2008 focusing on
118 the Midwest of the United States, and found that the nucleation resulted in decreased
119 CCN at low supersaturation ($SS=0.1\%$). Besides, a study carried out for East Asia in
120 2009 also indicated that at low supersaturation (e.g. $SS=0.1\%$), nucleation has little
121 impact on CCN (Matsui et al., 2013). The contrasting effects of nucleation on CCN at
122 low supersaturations in model and observations is not explained in these previous
123 studies.

124 At the stage of particle growth, secondary organic aerosol (SOA) formed by
125 atmospheric oxidation of organic vapors is a major contributor to particle growth to

126 CCN-related sizes (Liu and Matsui, 2022; Qiao et al., 2021). SOA formed by multi-
127 generational gas-phase oxidation of semi-volatile and intermediate volatility organic
128 compounds (S/IVOC) is called SI-SOA (Jimenez et al., 2009; Zhang et al., 2007). Zhao
129 et al. (2016) made a comprehensive assessment of the roles of various SOA precursors
130 in SOA formation in real atmosphere in China in 2010, and the results demonstrated
131 that evaporated POA and IVOC (i.e. S/IVOC) made a significant contribution to SOA,
132 contributing up to 82% to the average SOA concentration in eastern China. However,
133 the effect of SI-SOA on CCN has not been fully studied.

134 In this paper, WRF-Chem was applied to simulate the effect of the NPF on CCN
135 in China in February 2017. The simulated results from the WRF-Chem model are firstly
136 compared with observations in Qingdao, Beijing and Gucheng, exhibiting large biases
137 in CN. This is followed by an improvement through a few processes. At the end, the
138 impact of SI-SOA yield and nucleation on CCN is investigated.

139 **2. Data and methods**

140 **2.1 Observations**

141 The measurements used in this study were carried out over the sampling site from
142 February 5 to 24, 2017 at the campus of Ocean University of China (36°09'37"N,
143 120°29'44"E) in Qingdao, which is surrounded by residential buildings and is situated
144 about 10 km away from the city center. A fast mobility particle sizer (FMPS, TSI Model
145 3091) was applied to measure the aerosol particle size distribution for the size range of
146 5.6 nm to 560 nm (Liu et al., 2014b). The bulk CCN concentration is measured by a
147 cloud condensation nuclei counter at three different supersaturations (0.2%, 0.4% and
148 0.6%) and each supersaturation lasts for 20 minutes. More information about the CCN
149 measurement can be found in Li et al. (2015). The urban site in Beijing is located on
150 the roof of the building of the Chinese Academy of Meteorological Sciences (CAMS,
151 39°95'N, 116°33'E) in the campus of the China Meteorological Administration, close
152 to the main road with heavy traffic. The rural site is Gucheng (GC, 39°08'N, 115°40'E),
153 located in Hebei Province, surrounded by farmland, and is a representative station of
154 the severity of air pollution in Beijing Tianjin Hebei region. The particle number size
155 distribution of these two sites in the range of 4–850 nm is measured by a Tandem

156 Scanning Mobility Particle Sizer (TSMPS), and more information about the
 157 instruments can be found in Shen et al. (2018).

158 2.2 Model configurations

159 WRF-Chem version 3.9 is used to simulate NPF events, with the main physical
 160 and chemical parameterization settings summarized in Table 1. The spatial resolution
 161 is 36 km by 36 km with 35 vertical layers and a model top at 50 hPa. The regional
 162 model simulations at a higher spatial resolution may be desirable in future when urban
 163 pollution is focused. A continuous run from February 1 to 25, 2017, was conducted,
 164 with the first five-day results as the spin-up and discarded in the analysis.

165 Table 1 WRF-Chem model configurations used in this work

Model configuration	
Microphysics	Morrison 2-moment microphysics scheme (Morrison et al., 2009)
Planetary Boundary Layer (PBL)	YSU boundary layer scheme (Hong et al., 2006)
Longwave and Shortwave Radiation	RRTMG longwave and shortwave radiation
Land model	Unified Noah Land Surface scheme (Chen and Dudhia, 2000; Tewari et al., 2016)
Cumulus	Grell-3D cumulus parameterization scheme (Grell, 1993)
Aerosol module	MOSAIC module (Zaveri et al., 2008; Matsui et al., 2011)
Gas-phase Chemistry	SAPRC-99 gas-phase chemistry scheme (Carter, 2000)

166

167 The meteorological initial and boundary conditions are driven by Climate Forecast
 168 System model version 2 (CFSv2; (Saha et al., 2014)) reanalysis developed by National
 169 Centre for Environmental Prediction (NCEP). The initial and boundary chemical
 170 conditions of WRF-Chem are provided by Community Atmosphere Model with
 171 Chemistry (CAM-Chem; (Buchholz et al., 2019)). Anthropogenic emissions for the
 172 year of 2017 are obtained from the Multiresolution Emission Inventory for China
 173 (MEIC, <http://www.meicmodel.org/>) emission dataset (Li et al., 2017; Zheng et al.,

174 2018).

175 The Model for Simulating Aerosol Interactions and Chemistry (MOSAIC) was
176 used to delineate dynamic gas-particle mass transfer to represent the condensation
177 growth of aerosol (Zaveri et al., 2008). The gas-particle partitioning of gas species on
178 particles is regulated by the mass transfer rate, which is related to mass accommodation
179 coefficient (α), a parameter involved in the model representing the probability of gas
180 molecules entering the bulk liquid phase (Pöschl et al., 1998). The original setting of α
181 for all condensing species for all size bins a in MOSAIC is 0.1 (Zaveri et al., 2008). In
182 the default release of WRF-Chem, MOSAIC was implemented in the sectional
183 framework with aerosol size distributions divided into 4 or 8 size bins spanning 39 nm
184 to 10 μm in diameter. To explicitly express the nucleation and the growth of newly
185 formed particles, the aerosol size range in the MOSAIC module was extended from 1
186 nm to 10 μm , with the number of aerosol size bins increased to 20 (Matsui et al., 2011;
187 Matsui et al., 2013; Lupascu et al., 2015; Lai et al., 2022). The calculation method of
188 CCN concentration in the WRF-chem model is referred to the study of Matsui et al.
189 (2011). Based on Köhler theory, CCN concentrations under the three given
190 supersaturations of 0.2%, 0.4% and 0.6% were calculated. The critical supersaturation
191 (S_c) of each size bin in the WRF-chem model was calculated by the following formula:

$$192 \quad S_c = \sqrt{\frac{4 \times a^3}{27 \times r^3 \times \kappa}} \quad (1)$$

$$193 \quad a = \frac{2 \times \sigma}{R_v \times T \times \rho_w} \quad (2)$$

194 Where α (m) is the coefficient of the Kelvin effect, κ is the volume-averaged
195 hygroscopicity, calculated using these values in Table 1, r (m) is the dry diameter, σ is
196 droplet surface tension over water (0.076 N m^{-1}), R_v is the gas constant for water vapor
197 ($461.6 \text{ J K}^{-1}\text{kg}^{-1}$), T (K) is the air temperature, and ρ_w is the density of water (1000 kg
198 m^{-3}).

199

200

201

202

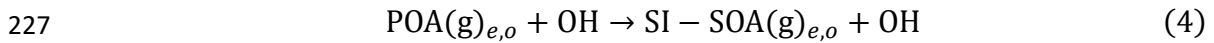
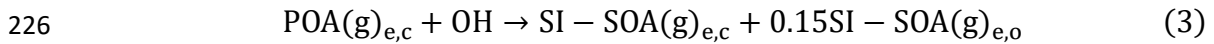
Table 2 Hygroscopicity Parameters (κ) in the WRF-Chem Model

Species	Hygroscopicity (κ)
Sulfate	0.5
Ammonium	0.5
Nitrate	0.5
Black carbon	10^{-6}
Primary organic aerosol	0.14
Other inorganics	0.14
Sodium	1.16
Chloride	1.16

203

204 The chemical aging process of organic aerosols (OA) is modeled by the volatility
 205 basis set (VBS) approach, which was widely used in air quality models to represent
 206 complex mixtures of thousands of organic species (Donahue et al., 2006; Shrivastava
 207 et al., 2011; Chrit et al., 2018). The VBS method classifies compounds according to the
 208 effective saturation concentration (c^*), which represents the proportion of the
 209 component in the gas phase to the particle phase (Donahue et al., 2006), and species
 210 with higher c^* values are more volatile. The oxidation of highly volatile precursors to
 211 form relatively low volatile components represents the aging process of OA. OA
 212 consists of directly emitted primary organic aerosols and photochemically produced
 213 secondary organic aerosols (SOA) (Shrivastava et al., 2011). In this study, the
 214 simplified 2-species VBS mechanism was applied to the simulation of SOA, during
 215 which primary organic aerosol was represented by two species based on volatility with
 216 effective saturation concentration c^* values (at 298 K and 1 atm) of 10^{-2} and $10^5 \mu\text{g}$
 217 m^{-3} (Shrivastava et al., 2011). Primary organic aerosols with c^* of $10^5 \mu\text{g m}^{-3}$ refers to
 218 S/IVOC, which is in the gas phase under most atmospheric conditions due to its high
 219 volatility, while for those primary organic matters with c^* of $10^{-2} \mu\text{g m}^{-3}$, is treated as
 220 gas phase as well in the original model. The SOA formed by photochemical oxidation
 221 of S/IVOC precursors is called SI-SOA and the SOA formed by oxidation of VOC
 222 precursors is named V-SOA. In the simplified 2-species VBS mechanism, SI-SOA (c^*

223 of $10^{-2}\mu\text{g m}^{-3}$) is formed by the oxidation reaction of S/IVOC precursors (c^* of $10^5\mu\text{g}$
224 m^{-3}) and OH with an oxidation rate constant of $4 \times 10^{-11} \text{ cm}^3 \text{ molec}^{-1} \text{ s}^{-1}$. The equations
225 for controlling the oxidation of S/IVOC precursors are as follows:



228 where POA(g) denotes primary organic aerosols with c^* of $10^5 \mu\text{g m}^{-3}$, which reacts
229 with OH to form SI-SOA(g) with c^* of $10^{-2} \mu\text{g m}^{-3}$. Subscripts c and o represent the
230 non-oxygen and oxygen parts respectively of given species and e is either the biomass
231 or anthropogenic emission sector. In addition, SVOC and IVOC emissions
232 corresponding to both anthropogenic and biomass burning emissions are derived based
233 on constant emission ratio of S/IVOC to POA (Shrivastava et al., 2011). A detailed
234 description of 2-species VBS mechanism can be found in Shrivastava et al. (2011).

235 **2.3 Model sensitivity formulations**

236 Three sets of sensitivity tests are designed and listed in Table3. The purposes of
237 the three sets of experiments are as follows: (1) Adjust the condensation growth process
238 of ultrafine particles in WRF-Chem model (Base, MAC, PEP, NOCD, RACD, with
239 details in Table 3); (2) Explore the effect of SI-SOA yield on CCN (Low_Yield and
240 High_Yield); (3) Study the effect of nucleation process on CCN under the change of
241 SI-SOA yield (Low_Yield and High_Yield and their corresponding cases without
242 nucleation parameterization, i.e., Low_nucoeff and High_nucoeff). Each scenario will be
243 explained in conjunctions with the results.

244
245
246
247
248
249
250
251
252
253
254

Table 3 The sensitivity tests involved in this study

Purposes	Simulation scenarios	Description
Adjust the condensation growth process of ultrafine particles	Base	Simulation with the default setting with nucleation coefficient set as $2 \times 10^{-6} \text{ s}^{-1}$, the same as Lai et al. (2022).
	Mass accommodation coefficient (MAC)	It is the same as Base except that the mass adjustment coefficient (α) of gaseous sulfuric acid is adjusted from 0.1 to 0.65.
	POA emission phase (PEP)	It is the same as MAC except that the phase of POA is changed from gas phase to particle phase.
	No condensation (NOCD)	It is the same as PEP except that no NH_4NO_3 condenses on particles below 40 nm.
	Ratio method for condensation (RACD)	It is the same as PEP except that the condensation of NH_4NO_3 on particles below 40 nm is reduced according to the ratio of acid particles to total particles reported in Wang et al. (2014).
Explore the effect of SI-SOA yield on CCN (Explore the effect of nucleation process on CCN under the change of SI-SOA yield)	High_Yield	Simulation with high oxidation rate of SI-SOA formation with reaction rate constant of $5 \times 10^{-11} \text{ cm}^3 \text{ molec}^{-1} \text{ s}^{-1}$
	Low_Yield	Simulation with low oxidation rate of SI-SOA formation with reaction rate constant of $2 \times 10^{-11} \text{ cm}^3 \text{ molec}^{-1} \text{ s}^{-1}$

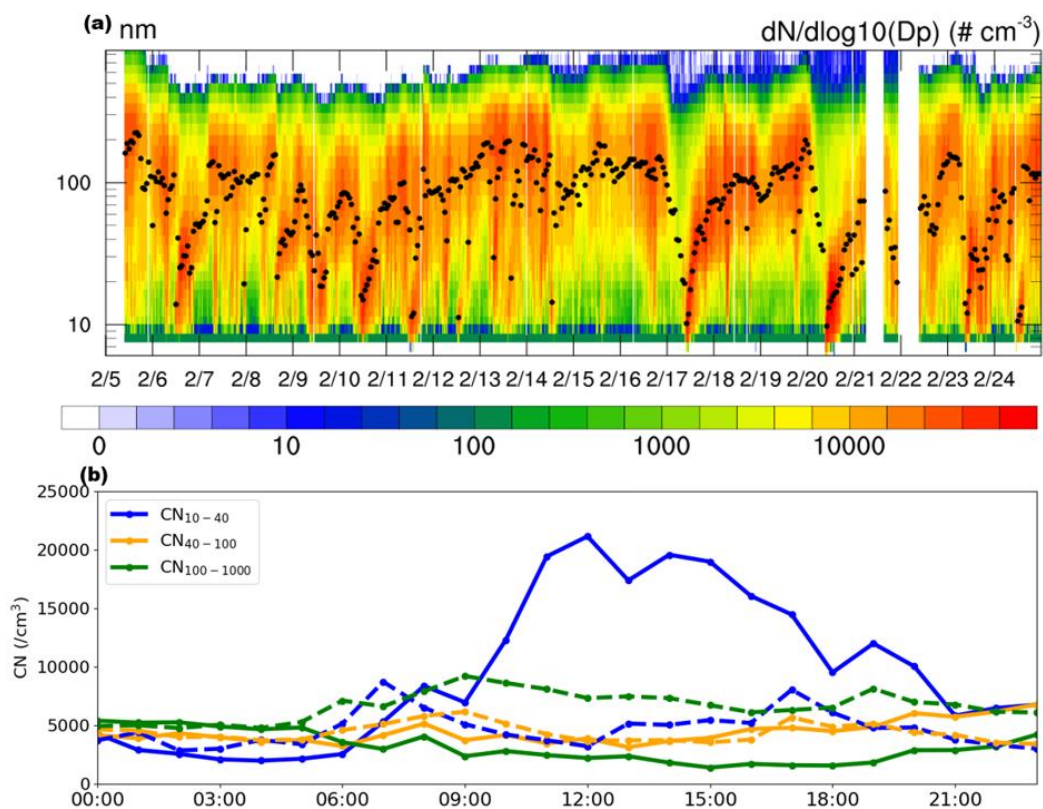
Explore the effect of nucleation process on CCN under the change of SI-SOA yield	High_NUCOFF Low_NUCOFF	Simulations without nucleation parameterizations based on High_Yield Simulations without nucleation parameterizations based on Low_Yield
--	---------------------------	---

256

257 **3. Results**

258 **3.1 Observational analysis**

259 Based on the criteria (Dal Maso et al., 2005; Kulmala et al., 2012), NPF is defined
 260 as an event with the emergence of a nucleation mode with particle diameters smaller
 261 than 25 nm, lasting for 2 hours or more, followed in general by a continuous particle
 262 growth. Six NPF events were identified in February 2017 in Qingdao, on the days of 6,
 263 9, 10, 17, 20 and 23 (Fig. 1a), yielding a frequency of ~30% and displaying a typical
 264 banana-shaped growth of particles in the particle number size distribution. Compared
 265 to a few other studies on NPF frequency in Qingdao, the results in this study are to a
 266 large extent consistent with that in the fall of 2012–2013 (30%; (Zhu et al., 2019)),
 267 slightly higher than that in summer 2016 (22%; (Zhu et al., 2019)) and lower than that
 268 in spring of 2010 (41%; (Liu et al., 2014b)). The higher frequency in spring in Qingdao
 269 is consistent with the observational results at different stations in the Northern
 270 Hemisphere in Nieminen et al. (2018).



271
 272 Fig. 1. Distribution of particle number concentration. (a) Temporal evolution of particle
 273 size distributions (colored shading) and geometric median diameter (GMD; dots in
 274 black) in Qingdao on February 5-24, 2017. (b) The mean diurnal variation of CN₁₀₋₄₀
 275 (blue), CN₄₀₋₁₀₀ (orange) and CN₁₀₀₋₁₀₀₀ (green) composited during the NPF (solid lines)
 276 and non-NPF (dashed lines) days on February 5-24, 2017. All times are local times (LT)
 277

278 During the six NPF events identified in February in Qingdao, the mean diurnal
 279 cycle of CN₁₀₋₄₀ (10–40 nm) particles exhibits triple peaks (solid blue in Fig. 1b), in the
 280 morning (8:00 LT), noon (12:00–14:00 LT) and evening (19:00 LT), respectively. A
 281 comparable three-peak feature was also observed in earlier years during 2016-2018 in
 282 Qingdao (Zhu et al., 2021). The morning and evening peaks of CN₁₀₋₄₀, with values of
 283 $\sim 5300 \text{ cm}^{-3}$ and $\sim 12000 \text{ cm}^{-3}$, respectively, are likely caused by the primary emissions
 284 from traffic and cooking activities (Wu et al., 2021a; Wang et al., 2022; Cai et al., 2020).
 285 The occurrence of NPF starts approximately at 9:00 am LT, accompanied by a
 286 substantial increase in CN₁₀₋₄₀ compared with non-NPF days (solid vs. dashed lines, in
 287 blue), yielding a peak around noon (20000 cm^{-3} during 12:00–14:00 LT). In addition,

288 larger particles (e.g., CN_{40–100} and CN_{100–1000}) displayed a slow or no increase in the
289 afternoon.

290

291 **3.2 Model improvement in particle number concentration simulations**

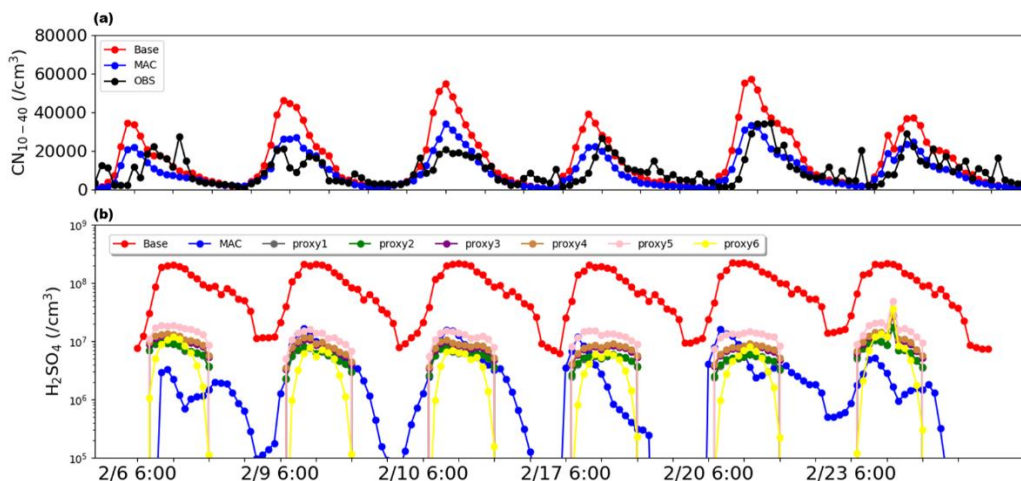
292 Particle number concentrations, primarily in two ranges of 10–40 nm and 40–100
293 nm, are commonly simulated with large biases. In the smaller size range (10–40 nm),
294 the particle number concentration is associated with NPF and particle growth. During
295 NPF, despite differences among the formation mechanisms, H₂SO₄ is considered the
296 common species (Yu, 2005; Lovejoy et al., 2004), which often suffer large biases (Cai
297 et al., 2016; Matsui et al., 2011). In the size range of 40–100 nm, the particle number
298 concentration is primarily affected by the condensation growth of particles below 40
299 nm, which is closely related to chemical components such as SOA and nitrate. Prior to
300 the evaluation of particle number concentration, we first evaluate the compositions of
301 PM_{2.5} and criteria air pollutants including PM_{2.5}, PM₁₀, O₃, SO₂, CO, and NO₂, showing
302 relatively low biases compared to observations (section S1 and Fig. S1 and Fig. S2 of
303 the supporting information).

304

305 **3.2.1 Bias correction of particle number concentration at 10–40 nm**

306 In this study, as shown in Fig. 2, comparisons of CN_{10–40} between simulations (red
307 line in Fig. 2a) and observations (black line in Fig. 2a) results of the six NPF events
308 mentioned in the previous section in Qingdao in February 2017 indicate that model
309 overestimates CN_{10–40} with mean fractional bias of 48%. As one of the major processes
310 affecting the particle number concentration of 10–40 nm, nucleation is governed by the
311 particle nucleation rate of 1 nm particles (cm⁻³ s⁻¹), which is closely associated with the
312 concentration of H₂SO₄. For instance, in a commonly applied activation mechanism,
313 the nucleation rate calculated by $J^* = K_{ACT} \times [H_2SO_4]$. Note that K_{ACT} is the nucleation
314 coefficient considering the physical properties and chemical species of nucleation
315 process under different environments, indicating that a lumped chemical species are
316 included in the scheme reflected primarily in the nucleation coefficient k, set as 2×10
317 $^{-6} \text{ s}^{-1}$ based on previous studies (Sihto et al., 2006; Riipinen et al., 2007). Dong et al.

318 (2019) simulated NPF occurring in the summer of 2008 in the United States using the
 319 NPF-explicit WRF-Chem based on the activation mechanism, which overestimated the
 320 particle number concentration at 10–63 nm by nearly doubled, even when the K_{ACT}
 321 decreased by one order of magnitude (set at a very low value of 10^{-7} s^{-1}). Therefore, it
 322 is likely that the overestimation of particle number concentration in the smaller particle
 323 size segment is probably due to the bias of simulated sulfuric acid.



324
 325 Fig. 2. Time series of (a) CN_{10-40} on NPF days, where red and blue represent Base and
 326 MAC simulation results respectively, and black represents observation results, and (b)
 327 sulfuric acid gas concentration obtained by simulation and by proxies (dark grey: Eq.
 328 5; green: Eq. 6; purple: Eq. 7; brown: Eq. 8; pink: Eq. 9; yellow: Eq. 10). All times are
 329 in local times.

330

331 Measurement of sulfuric acid gases in the lower troposphere is challenging due to
 332 the generally low ambient concentration of sulfuric acid (10^6 – 10^7 molecule cm^{-3}).
 333 Different methods have been proposed to estimate ambient sulfuric acid concentrations
 334 based on observations such as SO_2 (Petäjä et al., 2009; Lu et al., 2019; Mikkonen et al.,
 335 2011). For instance, Petäjä et al. (2009) proposed a linear method to approximate
 336 observed H_2SO_4 concentration in Hyytiälä, southern Finland. Moreover, a recent study
 337 by Lu et al. (2019) proposed a nonlinear method to construct a number of proxies for
 338 gaseous sulfuric acid concentration (Eq. 5–9), indicating that compared to the linear
 339 method in Petäjä et al. (2009), the nonlinear relationship can provide more accurate
 340 H_2SO_4 concentration in Beijing during February–March 2018 period. In addition, we

341 also used another sulfuric acid nonlinear proxy (Eq. 10) based on long-term
 342 observations in Germany, Finland, the United States, etc. (Mikkonen et al., 2011). In
 343 this study, we adopt the above six nonlinear proxy methods (referred as proxy5 to
 344 proxy10) to estimate H₂SO₄ in Qingdao.

$$345 \quad [H_2SO_4] = 515.74 \times [SO_2]^{0.38} \times \text{Radiation}^{0.14} \times CS^{0.03} \quad (5)$$

$$346 \quad [H_2SO_4] = 280.05 \cdot \text{Radiation}^{0.14} [SO_2]^{0.40} \quad (6)$$

$$347 \quad [H_2SO_4] = 9.95 \times [SO_2]^{0.39} \times \text{Radiation}^{0.13} \times CS^{-0.01} \times [O_3]^{0.14} \quad (7)$$

$$348 \quad [H_2SO_4] = 14.38 \times [SO_2]^{0.38} \times \text{Radiation}^{0.13} \times [O_3]^{0.14} \quad (8)$$

$$349 \quad [H_2SO_4] = 0.0013 \times [SO_2]^{0.38} \times \text{Radiation}^{0.13} \times CS^{-0.17} \times ([O_3]^{0.14} + [NO_x]^{0.41}) \quad (9)$$

$$350 \quad [H_2SO_4] = 8.21 \times 10^{-3} \times [SO_2]^{0.62} \times \text{Radiation} \times (CS \times RH)^{-0.13} \quad (10)$$

351 where [SO₂], [O₃] and [NO_x] (molecule cm⁻³) represents concentration of
 352 observed SO₂, O₃ and NO_x, respectively. “Radiation” (W m⁻²) is global radiation. RH
 353 (%) is the relative humidity, and CS (s⁻¹) is the condensation sink, which is calculated
 354 based on observed particle distribution.

355

356 The simulated H₂SO₄ concentration from the Base simulation (dots in Fig. 2b) is
 357 compared with observations obtained by proxies (see Fig. 2b), indicating that Base
 358 simulations apparently overestimate by one order of magnitude compared to the H₂SO₄
 359 estimated by proxies. The overestimation has been frequently reported previously, i.e.,
 360 over Beijing (Matsui et al., 2011), which ascribes the bias to the overestimation of the
 361 SO₂ concentration. In a more recent study, the sensitivity of H₂SO₄ to SO₂ is tested, and
 362 the result shows that even when SO₂ is reduced to an unrealistically low level, the
 363 simulated H₂SO₄ is still more than one order of magnitude higher than the observed
 364 value (Lai et al., 2022), suggesting that the SO₂ concentration cannot fully explain the
 365 overestimates.

366 In addition to the precursor of H₂SO₄, the mass accommodation coefficient (α),
 367 representing the probability of impaction of a gaseous molecule on a liquid surface and
 368 entering the bulk liquid phase, is another important factor affecting the concentration
 369 of sulfuric acid gas. In the public release of WRF-Chem, mass accommodation

370 coefficient is typically set to a low value of 0.1 for all gas species under different
371 volatility during the condensation process, including H₂SO₄ (Davidovits et al., 2004;
372 Zaveri et al., 2008). Recent studies indicate that the low mass accommodation
373 coefficient value may not be applicable to the low volatile gases, which tend to have a
374 mean mass accommodation coefficient value of 0.7 and close to the unity (Krechmer et
375 al., 2017). In fact, an earlier study has indicated based on experimental determination,
376 the mass accommodation coefficient of H₂SO₄ vapor in sulfuric acid aqueous solution
377 was measured, and the best fit value was 0.65. Accordingly, a sensitivity simulation was
378 conducted by adjusting the mass accommodation coefficient of H₂SO₄ from 0.1 to 0.65,
379 referred to as MAC.

380 This simulation brought the H₂SO₄ concentration (see Fig. 2b) much closer to the
381 calculated results from proxies, and the corresponding biases reduced by approximately
382 an order of magnitude. Notably, the MAC simulation decreases the overestimate of
383 sulfuric acid gas concentration, resulting in a lower particle formation rate. The MAC
384 simulation also significantly reduces overestimate of CN_{10–40} (Fig. 2a), and mean
385 fractional bias compared to observations decreases from 48% to 1%.

386

387 **3.2.2 Improvement of particle number concentration simulations at 40–100 nm**

388 The number concentration of particles in the 40–100 nm range is mainly affected
389 by the coagulation and condensation processes. While the coagulation process tends to
390 largely affect ultrafine particles below 10 nm than those with larger sizes (Wu et al.,
391 2011), the condensation growth of particles during gas-particle partitioning at sizes of
392 10–40 nm, to a large extent, governs the variations in number concentration of 40–100
393 nm particles. The condensation process is primarily controlled by gas-particle
394 partitioning of chemical species, which may change the chemical composition of
395 particles, such as organic compounds and inorganics including sulfate, nitrate and
396 ammonium.

397 Among the species contributing to the condensation growth of particles at 10–40
398 nm, the organic compounds with c^* of $10^{-2} \mu\text{g m}^{-3}$ play the dominant role (Pierce et al.,
399 2011). In the current model setting, the low volatile organic matter of $10^{-2} \mu\text{g m}^{-3}$ comes

400 from two gas-phase sources, including the direct emission of primary organic aerosol
401 (POA) and SOA formed from S/IVOC (SI-SOA), conducive to condensation on
402 particles. While the condensation of gaseous SOA is in general reasonable, the gas
403 phase emissions of POA may be problematic. For instance, previous studies suggested
404 that POA is in gas phase close to the emissions source. However, with rapid dilution
405 and cooling in the atmosphere away from the source, most POA condenses to particle-
406 phase (Roldin et al., 2011a; Roldin et al., 2011b; Shrivastava et al., 2008). Therefore,
407 away from the emissions source POA, being in the particle phase, will not be involved
408 in the growth of newly formed particles. Therefore, POA may not contribute to particle
409 growth away from the emission sources, which caused different size distributions of
410 POA compared to when it was emitted in the gas-phase (Fig. S3a vs. Fig. S3b). Emitting
411 low volatility POA in the particle phase eliminates the unreasonable quasi-banana shape
412 pattern exhibiting concomitant growth of newly formed particles with increasing mass
413 concentration of POA.

414 The composition analysis (Fig. S3c) in the 10–40 nm particles mass from the
415 model results indicates that organic compounds mentioned above only account for 21%
416 of total mass (sulfates, nitrates, ammonium salts and organics) in this size range and the
417 dominant species is nitrate which accounts for 51% of total mass, exhibiting
418 inconsistencies with the previous studies which in general indicates a much smaller
419 contribution of nitrate. For instance, Liu et al. (2014a) suggested that over North China
420 Plain in summer 2009, organic matter accounted for 77% of particles around 30 nm,
421 while the sum of SO_4^{2-} , NO_3^- and NH_4^+ only accounted for 18%. Recent observations
422 conducted in Beijing also indicated that particles at 8–40 nm are mainly composed of
423 organic matter (with mass fraction of ~80%) and sulfate (with mass fraction of ~13%),
424 while nitrate content is very low (with mass fraction of ~3%) (Li et al., 2022). Another
425 study showed that nitrate accounted for 7–8% at urban sites and 17% at rural sites for
426 particles mass in 7–30 nm in the United States in 2007 (Bzdek et al., 2012). Therefore,
427 the potentially too high modeled nitrate fraction in 10–40 nm in this study is tightly
428 associated with the condensation process, with the specific reasons explained below.

429 The condensation of nitric acid on particles is highly constrained by the particle

430 acidity. The acidity in smaller particles (i.e., 10–40 nm) tends to be higher than that in
431 large particles, primarily due to the larger condensation of H₂SO₄ (Lu et al., 2022), and
432 particles with sizes greater than 40 nm have a much weaker acidity or are nearly neutral.
433 For example, observed evidence has shown that acidic ultrafine particles account for a
434 large proportion of ultrafine particles from 22 December 2010 to 15 January 2011 in
435 Hong Kong, e.g., 65% for particles within 5.5–30 nm (Wang et al., 2014).

436 In the model, a particle is determined to be in solid phase when the ambient relative
437 humidity is lower than the mutual deliquescence relative humidity of the particles
438 (Zaveri et al., 2005; Zaveri et al., 2008), which is in general suitable for particles
439 dominated by inorganics. In the study area, the results indicate that at most conditions
440 relative humidity are relatively low and the particles are in solid phase, in which the
441 condensation process is not affected by particle acidity and the condensation of nitric
442 acid on particles is directly calculated based on the gas-particle equilibrium
443 concentration (Zaveri et al., 2008). However, for particles below 40 nm, the main
444 compositions are likely to be organic matter (Zhu et al., 2014; Ehn et al., 2014), which
445 tends to be in liquid phase (Virtanen et al., 2011; Cheng et al., 2015), under which the
446 condensation of nitric acid is strongly constrained by acidity. Therefore, the phase
447 misrepresentation ignores the weakening effect of acidity on nitric acid condensation,
448 resulting in too high nitrate therein.

449 To overcome this issue, we propose a ratio method for condensation (RACD) to
450 partition the condensation of nitric acid on particles under 40 nm, by applying a ratio
451 of the number concentration of non-acidic particles to ultrafine particles. The method
452 is based on two assumptions, including: 1) little condensation of nitric acid on particles
453 with strong acidity (Lu et al., 2022); 2) the condensation of nitric acid on particles is
454 proportional to the ratio of the number concentration of non-acidic ultrafine particles to
455 the total particles, despite the existence of uncertainties. Fig. S4 depicts the average
456 particle number concentration and acid particle in the 1 to 40 nm range, calculated based
457 on Wang et al. (2014). The ratio of non-acidic particles is 8% for particles below 10 nm,
458 18% for particles at 10–15.8 nm, 30% for particles at 15.8–25.1nm, and 55% for
459 particles at 25.1–39.8 nm (Fig. S4). Note that the ratio is based on measurements

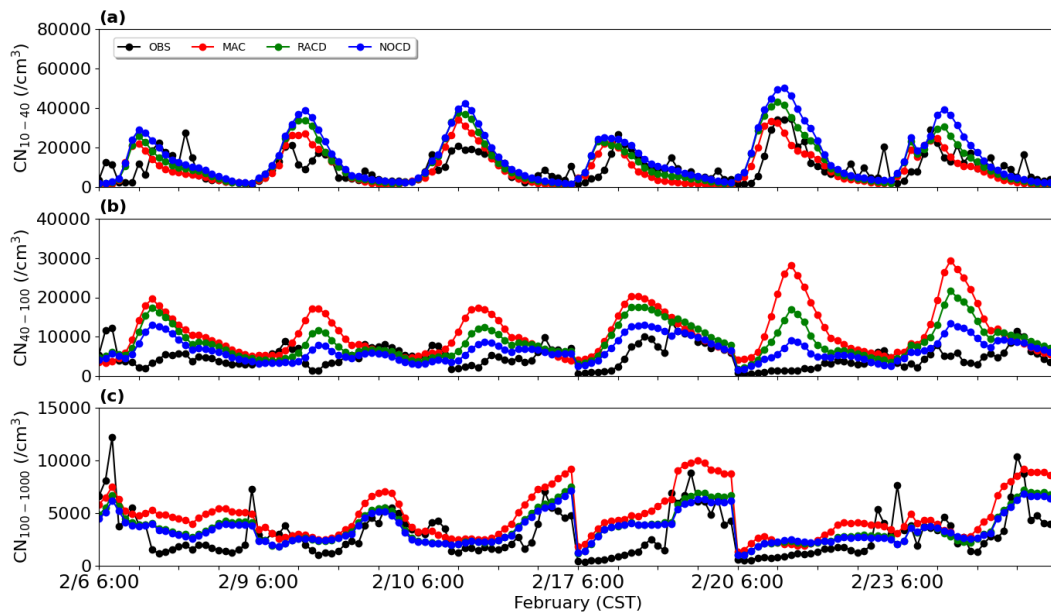
460 acquired at a single site in Hong Kong, therefore more observational studies are needed
461 to warrant the robustness of the method. Alternatively, the condensation of nitric acid
462 on particles in bins from 1 nm to 40 nm is completely suppressed, referred to as NOCD.

463 The simulation results based on the two methods (RACD and NOCD) are shown in
464 Fig. 3. Compared to MAC, RACD simulations reduce previously noted overestimation
465 of particle number concentration in the 40–100 nm size range (Fig. 3b), with the mean
466 fractional bias decreases from 83% to 63%. In addition to the amount of nitrate
467 condensation during particle growth mentioned above, the overestimation of particle
468 number concentrations in the 40–100 nm range may be attributed to nucleation process.
469 More specifically, in the H₂SO₄-H₂O binary nucleation mechanism used in this study,
470 when the concentration of sulfuric acid gas is reduced (Section 3.2.1), the resulting
471 decrease in nucleation rate leads to a slight decrease in particle number concentration
472 at 40–100 nm relative to Base (mean fractional bias from 98% to 83%). Apart from that,
473 it may also be related to the choice of nucleation parameterization scheme. For example,
474 using a global chemical transport model GEOS-Chem with a nucleation mechanism in
475 which formation rate is a function of the concentrations of sulfuric acid and low-
476 volatility organics, Yu et al. (2015) overestimated the concentration of particles in the
477 10–100 nm range by 161% at nine sites in the summer in North America. A possible
478 explanation for this overestimation was given by the uncertainty of the predicted
479 concentration of organic compounds involved in organics-mediated nucleation
480 parameterization. After they switched to another scheme of the ion-mediated nucleation
481 mechanism without organic matter, the number becomes 27% lower than the
482 observations (Yu et al., 2015). The test based on different schemes is beyond the scope
483 of the study, which is therefore not investigated.

484 Moreover, the overestimation of particles over 100 nm (CN_{100–1000}; Fig. 3c), which
485 have a strong influence on CCN, also decrease in the RACD simulation. Thus, the mean
486 fractional bias decreases from 25% (MAC) to 1%. Note that the slight increase of CN_{10–}
487 40 through the application of RACD, can be linked to the decrease of nitrate
488 condensation, and leads to weakened particle growth and enhanced particle number
489 concentration at 10–40 nm (Fig. 3a). The alternative method by completely removing

490 the nitrate condensation (NOCD) yields even better performance in particle number
 491 concentration of 40–100 nm (mean fractional bias of 34%), indicating the feasibility by
 492 reducing the nitrate condensation. The proportion of nitrate simulated by RACD is 23%,
 493 closer to values reported in past observations (Bzdek et al., 2011; Bzdek et al., 2012),
 494 while the nitrate (1%) in the scenario of NOCD seems to be too low. Considering the
 495 limited observational information obtained based on previous studies, RACD is applied
 496 in this study.

497 In addition to Qingdao, we evaluate the model performance over a few other sites,
 498 including one site over urban Beijing and the other one over the rural area of Gucheng,
 499 yielding consistent improvements in model simulations (Section S2; Fig. S5-S7).
 500 Moreover, we select another empirical scheme, e.g., kinetics, and one classical
 501 nucleation scheme, indicating the empirical scheme of activation scheme is in general
 502 a good option in this study (Section S2; Fig. S8-S10; Table S1-3).



503
 504 Fig. 3. The time series of (a) CN_{10-40} , (b) CN_{40-100} and (c) $CN_{100-1000}$ on NPF days in
 505 Qingdao on February 5-24 simulated from MAC (marked in red), NOCD (marked in
 506 blue) and RACD (marked in green) as well as from observations (OBS) (marked in
 507 black). All times are local times.

508
 509
 510
 511

512 **3.3 Substantial contributions of SI-SOA to CCN**

513 Compared with the original model setting, after adjusting the growth process of
514 ultrafine particles (RACD), the number concentration of particles tends to decrease,
515 especially for particles above 40 nm. Ultrafine particles above 40 nm are important
516 sources of CCN (Dusek et al., 2006), in this way, the number concentration of CCN
517 also tends to decline. In addition, in the Base case, we found that the model
518 overestimated $CCN_{0.4\%}$ and $CCN_{0.6\%}$, with mean fractional bias being 64% and 87%,
519 respectively. After adjusting the condensation growth process of ultrafine particles,
520 under high supersaturation (i.e., $CCN_{0.4\%}$ and $CCN_{0.6\%}$), the capability of the model in
521 reproducing the CCN is improved. RACD reduces the overestimation of $CCN_{0.4\%}$ and
522 $CCN_{0.6\%}$, with mean fractional bias reduced to 30% and 56%, respectively, although the
523 overestimates still exist (Fig. S11b, c). However, for low supersaturation (i.e., $CCN_{0.2\%}$),
524 the decrease of number concentration of CCN is too large, and mean fractional bias
525 decreases from 7% to -45% (Fig. S11a), therefore the bias will be further adjusted later.

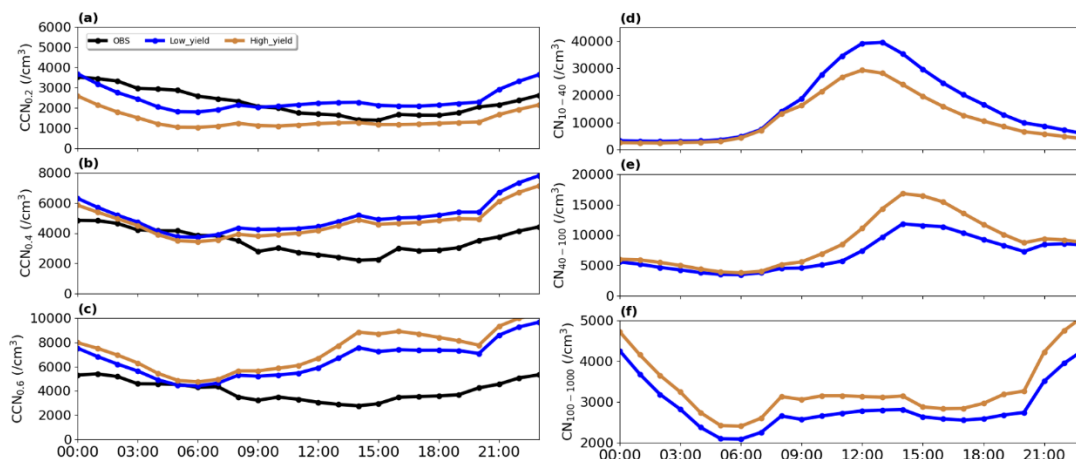
526 In addition to the growth process, the remaining overestimate of CCN under high
527 SS and underestimate of CCN over low SS is likely to be influenced by the chemical
528 compositions involved in the activation of ultrafine particles into CCN. Specifically,
529 ultrafine particles can grow up to CCN size under certain SS (Pierce and Adams, 2007).
530 This process is influenced by both particle size and hygroscopicity, and hygroscopicity
531 is closely related to the chemical composition of particles (Petters and Kreidenweis,
532 2007). In particular, inorganic compounds generally increase particle hygroscopicity,
533 increasing CCN. SOA has dual effects on CCN since it decreases particle
534 hygroscopicity but also promotes growth of particles, and these two effects are
535 competitive with each other (Wu et al., 2015; Zaveri et al., 2021). Ultrafine particles
536 must grow to a critical size to be activated into CCN (Dusek et al., 2006). SOA act as a
537 major contributor in promoting the condensational growth of ultrafine particles to the
538 critical size, facilitating particles activation into CCN. In contrast, SOA tends to reduce
539 the hygroscopicity of particles, leading to a diminished ability of activation to CCN
540 (Wu et al., 2015). These two competing effects work together and modulate the number

541 of CCN. Moreover, considering that SI-SOA is the main SOA component on ultrafine
542 particles (Fig. S11d), the effect of SI-SOA on CCN is therefore explored in this study.

543 Considering SI-SOA is a product of S/IVOC oxidation, the oxidation rate of
544 S/IVOC is tightly associated with CCN, which likely affects the bias of CCN. In the
545 original model setup, the oxidation rate is set to be a constant of $4 \times 10^{-11} \text{ cm}^3 \text{ molec}^{-1}$
546 s^{-1} for all S/IVOC. However, a recent study (Wu et al., 2021b) proposed that the
547 oxidation rate can be as high as $5 \times 10^{-11} \text{ cm}^3 \text{ molec}^{-1} \text{ s}^{-1}$ such as for polycyclic aromatic
548 hydrocarbons (PAHs), close to the original model value, but can be as low as half (i.e.,
549 $2 \times 10^{-11} \text{ cm}^3 \text{ molec}^{-1} \text{ s}^{-1}$) of the original modeling setting for S/IVOC species except
550 PAHs (O-S/IVOCs). It is noteworthy that the oxidation rates of 5×10^{-11} and 2×10^{-11}
551 in general represent the upper and lower bounds (Zhao et al., 2016; Wu et al., 2021b).

552 To delve into how oxidation rate affects CCN, we set up a few numerical
553 experiments (Table 3) to investigate the response of CCN to the oxidation rate of
554 S/IVOC at three supersaturations (0.6%, 0.4%, 0.2%), including cases of High_Yield
555 and Low_Yield. As it is shown in Fig. 4, decreasing the oxidation rate (Low_Yield)
556 leads to a reduction of $\sim 10\%$ of CCN at high supersaturation (i.e., CCN_{0.6%}) as
557 compared to the High_Yield simulation. This behaviour is a consequence of the
558 decrease of particle number concentrations associated with Low_Yield, particular of
559 the particles close to the critical diameter (40–100 nm). In this case, the effect of particle
560 size dominates the hygroscopicity. In contrast, at a lower supersaturation (CCN_{0.2%}),
561 CCN increases by 42% when the oxidation rate is switched from a high to a low value,
562 which is due to the smaller fraction of SI-SOA contributing to particulate mass when
563 the oxidation rate is low. In this case, relative to SOA, a larger fraction of other particle
564 constituents such as inorganics, increase the volume weighted particle hygroscopicity
565 (Dusek et al., 2006) which causes the increase of CCN number. This means that the
566 effect of hygroscopicity on CCN surpasses the influence on particle size at low
567 supersaturations. This conclusion is consistent with the observation conducted by Ma
568 et al. (2016) in the North China Plain in 2013, which suggested that along with the
569 decrease of SS, the particles that can be activated to CCN is more sensitive to changes
570 of particle hygroscopicity. Similarly, based on observational data in northern China in

571 summer, Wang et al. (2023) found that CN in 2020 is lower than that in 2014 due to
 572 particulate pollution control, however, the particles become more easily activated,
 573 attributable to the larger extent of decrease in organic matters compared to inorganics,
 574 leading to enhanced particle hygroscopicity and more conducive to activation.



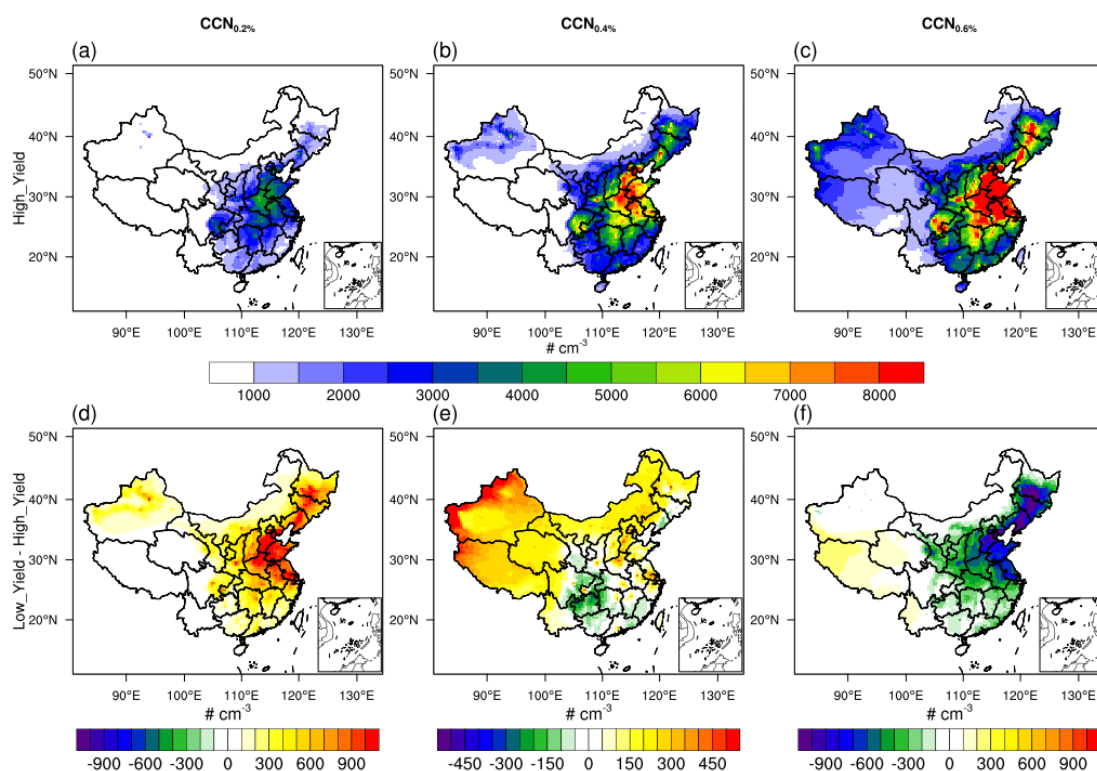
575
 576 Fig. 4. Average diurnal variation of (a) $CCN_{0.2\%}$, (b) $CCN_{0.4\%}$ and (c) $CCN_{0.6\%}$ and (d)
 577 CN_{10-40} , (e) CN_{40-100} , (f) $CN_{100-1000}$ on NPF days in Qingdao on February 5-24, 2017,
 578 in Low_yield and High_yield simulations, shown as blue and brown lines, and black
 579 lines represent observation results.

580

581 Furthermore, compared to the high yield of SI-SOA, the low SI-SOA yield results
 582 in a high CCN concentration under low SS and low CCN concentration under high SS.
 583 Therefore, both the underestimates of $CCN_{0.2\%}$ (mean fractional bias of -45%) and
 584 overestimates of $CCN_{0.6\%}$ (mean fractional bias of 56%) mentioned above are improved,
 585 with mean fractional bias of $CCN_{0.2\%}$ and $CCN_{0.6\%}$ reaching 7% and 43%, respectively
 586 (Fig. 4a, c). This result suggests that the oxidation rate of S/IVOC is possibly closer to
 587 the low value, which is understandable based on Wu et al. (2021b), who found that the
 588 amount of O-S/IVOCs, which corresponds to a low oxidation rate, is in general much
 589 larger (i.e., 20 times) than that of PAHs with a high oxidation rate.

590 In addition to the single site of Qingdao, we further explore the impact of SI-SOA
 591 yield on CCN from a larger spatial coverage (Fig. 5). Consistent with the mechanism
 592 revealed over Qingdao, even from a larger spatial perspective, a lower oxidation rate of

593 S/IVOC essentially enhances CCN at a lower SS (e.g., $CCN_{0.2\%}$; Fig. 5a) with the
594 highest increase over North China Plain area (Fig. 5a), and weakens CCN (i.e., by 10–
595 20% over Beijing-Tianjin-Hebei) at a higher SS (Fig. 5c), particularly over the dense
596 emission area (Fig. S12). It is worth noting that in the 2-species VBS mechanism used
597 in our study, all S/IVOC in the inventory is calculated based on a constant emission
598 ratio of S/IVOC to POA from all source categories (Shrivastava et al., 2011), which
599 may miss part of S/IVOC due to different emission ratios of POA from different source
600 (Chang et al., 2022). In addition, the simplified VBS mechanism used in our study does
601 not take into account the multi-step oxidation of organic species, which may introduce
602 some uncertainties. To be more specific, in the 2-species VBS mechanism, SI-SOA with
603 effective saturation concentrations (c^*) of $10^{-2} \mu\text{g m}^{-3}$ is formed by the vapor phase
604 oxidation of S/IVOC vapors with c^* of $10^5 \mu\text{g m}^{-3}$, reducing volatility by 7 orders of
605 magnitude. The process of one-step oxidation does not mean to represent a physical
606 process, but to parameterize the mean effect of a complex process of SOA formation
607 (Shrivastava et al., 2011). However, in the real atmosphere, the gaseous VOCs often
608 undergo multi-generational oxidation to form SOA (Garmash et al., 2020), during
609 which the properties and composition of SOA change substantially. For instance, by
610 adding the formation chemistry associated with multi-generational oxidation, Zhao et
611 al. (2020) found improved simulations of vertical aerosol profile in the Amazon free
612 troposphere compared to the simplified VBS mechanism.



613

614 Fig. 5. Spatial distributions of CCN concentrations at different supersaturations (SS),
 615 (a) and (d) are $CCN_{0.2\%}$, (b) and (e) are $CCN_{0.4\%}$, and (c) and (f) are $CCN_{0.6\%}$. The top
 616 panels exhibit the results from the High_Yield simulation, and the bottom panels shows
 617 the difference between the Low_Yield and High_Yield simulations.

618

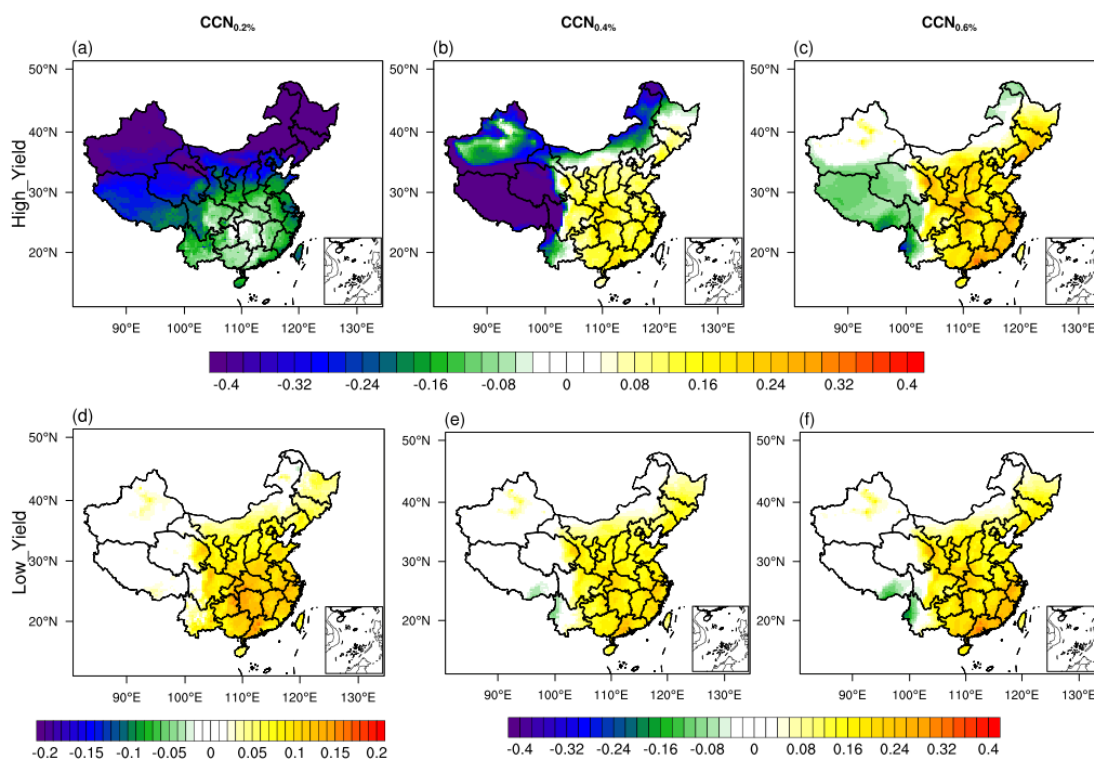
619 3.4 Contribution of nucleation to CCN under different SI-SOA yields

620 Considering the importance of nucleated particles on CCN (Yu et al., 2020;
 621 Westervelt et al., 2013), we further investigate the influence of nucleation on CCN
 622 under different SI-SOA yield conditions discussed above.

623 As shown in Fig. 6, in simulations close to the original model setting (High_Yield),
 624 when SS is low (i.e., $SS=0.2\%$), the nucleation process tends to reduce the CCN by
 625 $\sim 10\text{--}50\%$. In contrast, when the SS is high (0.6%), the nucleation results in a significant
 626 increase in CCN in most regions of China. When the yield of SI-SOA is adjusted to a
 627 lower level, the nucleation process has a positive contribution to CCN under both low
 628 and high SS. Especially, when SS is low (0.2%), the sign reversal, i.e., from negative
 629 (Fig. 6a) to positive (Fig. 6d) contributions of NPF to CCN along with the decrease of
 630 SI-SOA yield, i.e., the increase is concentrated in the eastern China with an average of

631 10–20%. The primary mechanism lies in that along with the decrease of SI-SOA yield,
 632 the smaller fraction of SI-SOA yields an increase in hygroscopicity, which surpasses
 633 the suppression effect on particle growth due to reduced SI-SOA formation. In the real
 634 atmosphere, when the supersaturation is usually low, e.g. about ~0.1% in polluted areas
 635 (Kalkavouras et al., 2019; Hudson and Noble, 2014), CCN will likely reduce with
 636 increasing oxidation rate of S/IVOC and corresponding SI-SOA formation.

637



638

639 Fig. 6. Spatial distribution of contribution of nucleation to CCN calculated by the ratio
 640 of the difference between the parameterization with and without nucleation to the
 641 parameterization with nucleation under different SI-SOA yields in China in February
 642 2017. (a), (d) is CCN_{0.2%}, (b), (e) is CCN_{0.4%}, (c), (f) is CCN_{0.6%}. The upper panel and
 643 lower panel represent High_Yield and Low_Yield simulation respectively

644

645 In addition to the linear-H₂SO₄ nucleation mechanism, one more empirical scheme
 646 of kinetics nucleation is selected, which assumes that the nucleation rate is proportional
 647 to the square of the concentration of sulfuric acid ($J = K[\text{H}_2\text{SO}_4]^2$), to investigate the
 648 effect of nucleation on CCN. Substantially positive contributions of nucleation to CCN

649 is found when the low SI-SOA yield is applied, consistent with what was shown based
650 on the linear-H₂SO₄ nucleation scheme (Fig. S13). However, nucleation contributes
651 positively to CCN even when the SI-SOA yield is high in the quadratic-H₂SO₄
652 nucleation scheme (e.g., kinetics nucleation scheme). When more sulfuric acid
653 molecules participate in nucleation under this scheme than the linear-H₂SO₄ nucleation
654 scheme, the particles are more easily hygroscopically activated to CCN, which is
655 equivalent to the effect of a reduction in organic components in the linear-H₂SO₄
656 nucleation scheme (e.g., activation-type nucleation scheme). The results from this study
657 show the importance of assessing the simulated effects of the nucleation scheme on not
658 only the formation and growth process of particles but also climate factors such as CCN
659 using observations.

660

661 **Conclusions and discussions**

662 In this study, WRF-Chem explicit-NPF simulations, with linear-H₂SO₄ nucleation
663 scheme (e.g., activation-type nucleation scheme), are used to investigate the observed
664 wintertime NPF events and their contribution to CCN in China. Based on observations
665 in a typical coastal city of Qingdao, as well as in the cities of Beijing and Gucheng over
666 North China Plain, we identify high biases of the model simulated CN and CCN
667 concentrations. Therefore, we updated and improved the parameterization setting on
668 particle growth in the model, mainly including: (1) adjusting the mass accommodation
669 coefficient (α) to from the default value of 0.1 to 0.65, an important parameter for
670 sulfuric acid condensation; (2) proportionally reducing the condensation amount of
671 nitric acid on particles below 40 nm; (3) changing the emitted low-volatility POA from
672 gas to particle. Through these adjustments, the capability of the model in reproducing
673 CN and CCN is substantially improved, leading to better agreement with the observed
674 results, which significantly reduces the overestimation of CN₁₀₋₄₀ (mean fractional bias
675 decreases from 48% to 1%) and CN₄₀₋₁₀₀ (mean fractional bias decreases from 98% to
676 63%).

677

678 For CCN, due to the crucial role of SI-SOA in promoting the growth of ultrafine
679 particles, on the basis of previous studies, we lower the oxidation rate of S/IVOC and
680 hence the production rate of SI-SOA, which weakens the growth of particles to reach
681 the critical size of CCN activation, but enhances particulate hygroscopicity favoring the
682 activation to CCN. When the yield of SI-SOA is adjusted to the lower bound of
683 literature value, $CCN_{0.6\%}$ is reduced by $\sim 10\%$ and is closer to observations. At low SS
684 ($CCN_{0.2\%}$), the decrease of SI-SOA yield has greater effects on the increase of particle
685 hygroscopicity compared to the effect of the reduction of particle size due to the
686 decrease of condensation growth. It results in an increase of CCN (as large as $\sim 42\%$) in
687 better agreement with observations. Under low SS conditions, common in the
688 atmosphere, a 2.5-fold reduction in SI-SOA yield results in a substantial increase of
689 CCN that switches from a negative contribution of new particle formation to CCN from
690 $-50\% \sim -10\%$ to a positive contribution of $10 \sim 20\%$.

691 In addition to activation nucleation scheme, we have also tested a few other
692 schemes such as the quadratic- H_2SO_4 nucleation scheme (e.g., kinetics nucleation
693 scheme). Under this scheme, the bias-corrected method abovementioned is applicable
694 to improving the simulations of concentrations of CN and CCN. It is noteworthy that
695 the dependence of CCN on the SI-SOA yield is diminished, showing that under both
696 high and low yields of SI-SOA, there are positive contributions of NPF to CCN. This
697 is likely due to the increase in the amount of sulfuric acid involved in nucleation,
698 making it more hygroscopic and easier to activate to CCN, and the high content of
699 inorganic species makes them less sensitive to changes in SI-SOA yield, which deserves
700 further investigation.

701

702 **Competing interests.** At least one of the (co-)authors is a member of the editorial board
703 of Atmospheric Chemistry and Physics.

704

705 **Acknowledgements.** This research was supported by grants from the National Natural
706 Science Foundation of China (42122039) and Fundamental Research Funds for the
707 Central Universities (202072001). Y.W. was supported by the National Science

708 Foundation Atmospheric Chemistry Program. M.S. was supported by the U.S.
709 Department of Energy (DOE) Office of Science, Office of Biological and
710 Environmental Research (BER) through the Early Career Research Program and the
711 Atmospheric System Research (ASR) program.

712

713 **References:**

714 Arghavani, S., Rose, C., Banson, S., Lupascu, A., Gouhier, M., Sellegri, K., Planche, C.: The Effect of
715 Using a New Parameterization of Nucleation in the WRF-Chem Model on New Particle
716 Formation in a Passive Volcanic Plume, *Atmosphere*, 13, 15, 2022.

717 Buchholz, R. R., Emmons, L. K., Tilmes, S.: The CESM2 Development Team., 2019. CESM2.1/CAM-
718 Chem Instantaneous Output for Boundary Conditions. UCAR/NCAR - Atmospheric Chemistry
719 Observations and Modeling Laboratory., doi: 10.5065/NMP7-EP60, 2019.

720 Bzdek, B., Zordan, C., Luther, G., Johnston, M.: Nanoparticle Chemical Composition During New
721 Particle Formation, *Aerosol Sci Technol*, 45, 1041-1048, doi: 10.1080/02786826.2011.580392,
722 2011.

723 Bzdek, B. R., Zordan, C. A., Pennington, M. R., Luther, G. W., III, Johnston, M. V.: Quantitative
724 Assessment of the Sulfuric Acid Contribution to New Particle Growth, *Environ. Sci. Technol.*,
725 46, 4365-4373, doi: 10.1021/es204556c, 2012.

726 Cai, C., Zhang, X., Wang, K., Zhang, Y., Wang, L., Zhang, Q., Duan, F., He, K., Yu, S.-C.: Incorporation
727 of new particle formation and early growth treatments into WRF/Chem: Model improvement,
728 evaluation, and impacts of anthropogenic aerosols over East Asia, *Atmospheric Environ.*, 124,
729 262-284, doi: <https://doi.org/10.1016/j.atmosenv.2015.05.046>, 2016.

730 Cai, J., Chu, B., Yao, L., Yan, C., Heikkinen, L. M., Zheng, F., Li, C., Fan, X., Zhang, S., Yang, D., Wang,
731 Y., Kokkonen, T. V., Chan, T., Zhou, Y., Dada, L., Liu, Y., He, H., Paasonen, P., Kujansuu, J. T.,
732 Petäjä, T., Mohr, C., Kangasluoma, J., Bianchi, F., Sun, Y., Croteau, P. L., Worsnop, D. R.,
733 Kerminen, V. M., Du, W., Kulmala, M., Daellenbach, K. R.: Size-segregated particle number
734 and mass concentrations from different emission sources in urban Beijing, *Atmos. Chem. Phys.*,
735 20, 12721-12740, doi: 10.5194/acp-20-12721-2020, 2020.

736 Carter, W.: Documentation of the SAPRC-99 Chemical Mechanism for VOC Reactivity Assessment,
737 Final Report to California Air Resources Board, 2000.

738 Chang, X., Zhao, B., Zheng, H., Wang, S., Cai, S., Guo, F., Gui, P., Huang, G., Wu, D., Han, L., Xing, J.,
739 Hanyang, M., Hu, R., Liang, C., xu, Q., Xionghui, Q., Ding, D., Liu, K., Han, R., Donahue, N.:
740 Full-volatility emission framework corrects missing and underestimated secondary organic
741 aerosol sources, *One Earth*, 5, 403-412, doi: 10.1016/j.oneear.2022.03.015, 2022.

742 Chen, F., Dudhia, J.: Coupling an Advanced Land-Surface/Hydrology Model with the Penn State/NCAR
743 MM5 Modeling System, 129, 2000.

744 Cheng, Y., Su, H., Koop, T., Mikhailov, E., Pöschl, U.: Size dependence of phase transitions in aerosol
745 nanoparticles, *Nat. Commun.*, 6, 5923, doi: 10.1038/ncomms6923, 2015.

746 Chrit, M., Sartelet, K., Sciare, J., Majdi, M., Nicolas, J., Petit, J. E., Dulac, F.: Modeling organic aerosol
747 concentrations and properties during winter 2014 in the northwestern Mediterranean region,
748 *Atmos. Chem. Phys.*, 18, 18079-18100, doi: 10.5194/acp-18-18079-2018, 2018.

749 Chu, B., Kerminen, V. M., Bianchi, F., Yan, C., Petäjä, T., Kulmala, M.: Atmospheric new particle
750 formation in China, *Atmos. Chem. Phys.*, 19, 115-138, doi: 10.5194/acp-19-115-2019, 2019.

751 Dal Maso, M., Kulmala, M., Riipinen, I., Wagner, R.: Formation and growth of fresh atmospheric
752 aerosols: Eight years of aerosol size distribution data from SMEAR II, Hyytiälä, Finland, *Boreal*
753 *Environ. Res.*, 10, 323-336, 2005.

754 Davidovits, P., Worsnop, D. R., Jayne, J. T., Kolb, C. E., Winkler, P., Vrtala, A., Wagner, P. E., Kulmala,
755 M., Lehtinen, K. E. J., Vesala, T., Mozurkewich, M.: Mass accommodation coefficient of water
756 vapor on liquid water, *Geophys. Res. Lett.*, 31, doi: <https://doi.org/10.1029/2004GL020835>,
757 2004.

758 Donahue, N. M., Robinson, A. L., Stanier, C. O., Pandis, S. N.: Coupled Partitioning, Dilution, and
759 Chemical Aging of Semivolatile Organics, *Environ. Sci. Technol.*, 40, 2635-2643, doi:
760 10.1021/es052297c, 2006.

761 Dong, C., Matsui, H., Spak, S., Kalafut-Pettibone, A., Stanier, C.: Impacts of New Particle Formation on
762 Short-term Meteorology and Air Quality as Determined by the NPF-explicit WRF-Chem in the
763 Midwestern United States, *Aerosol Air Qual Res*, 19, 204-220, doi: 10.4209/aaqr.2018.05.0163,
764 2019.

765 Dusek, U., Frank, G. P., Hildebrandt, L., Curtius, J., Schneider, J., Walter, S., Chand, D., Drewnick, F.,
766 Hings, S., Jung, D., Borrmann, S., Andreae, M. O.: Size Matters More Than Chemistry for
767 Cloud-Nucleating Ability of Aerosol Particles, *Science*, 312, 1375-1378, doi:
768 doi:10.1126/science.1125261, 2006.

769 Ehn, M., Thornton, J., Kleist, E., Sipilä, M., Junninen, H., Pullinen, I., Springer, M., Rubach, F., Tillmann,
770 R., Lee, B., Lopez-Hilfiker, F., Andrés, S., Acir, I. H., Rissanen, M., Jokinen, T., Schobesberger,
771 S., Kangasluoma, J., Kontkanen, J., Nieminen, T., Mentel, T.: A large source of low-volatility
772 secondary organic aerosol, *Nature*, 506, 476-479, doi: 10.1038/nature13032, 2014.

773 Fanourgakis, G. S., Kanakidou, M., Nenes, A., Bauer, S. E., Bergman, T., Carslaw, K. S., Grini, A.,
774 Hamilton, D. S., Johnson, J. S., Karydis, V. A., Kirkevåg, A., Kodros, J. K., Lohmann, U., Luo,
775 G., Makkonen, R., Matsui, H., Neubauer, D., Pierce, J. R., Schmale, J., Stier, P., Tsigaridis, K.,
776 van Noije, T., Wang, H., Watson-Parris, D., Westervelt, D. M., Yang, Y., Yoshioka, M.,
777 Daskalakis, N., Decesari, S., Gysel-Beer, M., Kalivitis, N., Liu, X., Mahowald, N. M.,
778 Myriokefalitakis, S., Schrödner, R., Sfakianaki, M., Tsimpidi, A. P., Wu, M., Yu, F.: Evaluation
779 of global simulations of aerosol particle and cloud condensation nuclei number, with
780 implications for cloud droplet formation, *Atmos. Chem. Phys.*, 19, 8591-8617, doi:
781 10.5194/acp-19-8591-2019, 2019.

782 Grell, G. A.: Prognostic Evaluation of Assumptions Used by Cumulus Parameterizations, *Mon Weather*
783 *Rev*, 121, 764-787, doi: 10.1175/1520-0493(1993)121<0764:PEOAUB>2.0.CO;2, 1993.

784 Guo, S., Hu, M., Zamora, M. L., Peng, J., Shang, D., Zheng, J., Du, Z., Wu, Z., Shao, M., Zeng, L.,
785 Molina, M. J., Zhang, R.: Elucidating severe urban haze formation in China, *Proc. Natl. Acad.*
786 *Sci. U.S.A.*, 111, 17373-17378, doi: doi:10.1073/pnas.1419604111, 2014.

787 Hong, S.-Y., Noh, Y., Dudhia, J.: A New Vertical Diffusion Package with an Explicit Treatment of
788 Entrainment Processes, *Mon Weather Rev*, 134, doi: 10.1175/MWR3199.1, 2006.

789 Hudson, J., Noble, S.: CCN and Vertical Velocity Influences on Droplet Concentrations and
790 Supersaturations in Clean and Polluted Stratus Clouds, *J Atmos Sci*, 71, 312-331, doi:
791 10.1175/JAS-D-13-086.1, 2014.

792 Jimenez, J. L., Canagaratna, M. R., Donahue, N. M., Prevot, A. S. H., Zhang, Q., Kroll, J. H., DeCarlo,
793 P. F., Allan, J. D., Coe, H., Ng, N. L., Aiken, A. C., Docherty, K. S., Ulbrich, I. M., Grieshop, A.
794 P., Robinson, A. L., Duplissy, J., Smith, J. D., Wilson, K. R., Lanz, V. A., Hueglin, C., Sun, Y.
795 L., Tian, J., Laaksonen, A., Raatikainen, T., Rautiainen, J., Vaattovaara, P., Ehn, M., Kulmala,
796 M., Tomlinson, J. M., Collins, D. R., Cubison, M. J., E, Dunlea, J., Huffman, J. A., Onasch, T.
797 B., Alfarra, M. R., Williams, P. I., Bower, K., Kondo, Y., Schneider, J., Drewnick, F., Borrmann,
798 S., Weimer, S., Demerjian, K., Salcedo, D., Cottrell, L., Griffin, R., Takami, A., Miyoshi, T.,
799 Hatakeyama, S., Shimojo, A., Sun, J. Y., Zhang, Y. M., Dzepina, K., Kimmel, J. R., Sueper, D.,
800 Jayne, J. T., Herndon, S. C., Trimborn, A. M., Williams, L. R., Wood, E. C., Middlebrook, A.
801 M., Kolb, C. E., Baltensperger, U., Worsnop, D. R.: Evolution of Organic Aerosols in the
802 Atmosphere, *Science*, 326, 1525-1529, doi: 10.1126/science.1180353, 2009.

803 Kalkavouras, P., Bougiatioti, A., Kalivitis, N., Stavroulas, I., Tombrou, M., Nenes, A., Mihalopoulos, N.:
804 Regional new particle formation as modulators of cloud condensation nuclei and cloud droplet
805 number in the eastern Mediterranean, *Atmos. Chem. Phys.*, 19, 6185-6203, doi: 10.5194/acp-
806 19-6185-2019, 2019.

807 Kerminen, V.-M., Chen, X., Vakkari, V., Petäjä, T., Kulmala, M., Bianchi, F.: Atmospheric new particle
808 formation and growth: Review of field observations, *Environ. Res. Lett.*, 13, doi: 10.1088/1748-
809 9326/aadf3c, 2018.

810 Krechmer, J. E., Day, D. A., Ziemann, P. J., Jimenez, J. L.: Direct Measurements of Gas/Particle
811 Partitioning and Mass Accommodation Coefficients in Environmental Chambers, *Environ Sci
812 Technol*, 51, 11867-11875, doi: 10.1021/acs.est.7b02144, 2017.

813 Kulmala, M., Dada, L., Daellenbach, K. R., Yan, C., Stolzenburg, D., Kontkanen, J., Ezhova, E., Hakala,
814 S., Tuovinen, S., Kokkonen, T. V., Kurppa, M., Cai, R., Zhou, Y., Yin, R., Baalbaki, R., Chan,
815 T., Chu, B., Deng, C., Fu, Y., Ge, M., He, H., Heikkinen, L., Junninen, H., Liu, Y., Lu, Y., Nie,
816 W., Rusanen, A., Vakkari, V., Wang, Y., Yang, G., Yao, L., Zheng, J., Kujansuu, J., Kangasluoma,
817 J., Petäjä, T., Paasonen, P., Järvi, L., Worsnop, D., Ding, A., Liu, Y., Wang, L., Jiang, J., Bianchi,
818 F., Kerminen, V.-M.: Is reducing new particle formation a plausible solution to mitigate
819 particulate air pollution in Beijing and other Chinese megacities?, *Faraday Discuss.*, 226, 334-
820 347, doi: 10.1039/D0FD00078G, 2021.

821 Kulmala, M., Laakso, L., Lehtinen, K. E. J., Riipinen, I., Dal Maso, M., Anttila, T., Kerminen, V. M.,
822 Hörrak, U., Vana, M., Tammet, H.: Initial steps of aerosol growth, *Atmos. Chem. Phys.*, 4, 2553-
823 2560, doi: 10.5194/acp-4-2553-2004, 2004.

824 Kulmala, M., Petäjä, T., Ehn, M., Thornton, J., Sipilä, M., Worsnop, D. R., Kerminen, V.-M.: Chemistry
825 of Atmospheric Nucleation: On the Recent Advances on Precursor Characterization and
826 Atmospheric Cluster Composition in Connection with Atmospheric New Particle Formation,
827 *Annu Rev Phys Chem*, 65, doi: 10.1146/annurev-physchem-040412-110014, 2013.

828 Kulmala, M., Petäjä, T., Nieminen, T., Sipilä, M., Manninen, H. E., Lehtipalo, K., Dal Maso, M., Aalto,
829 P. P., Junninen, H., Paasonen, P., Riipinen, I., Lehtinen, K. E. J., Laaksonen, A., Kerminen, V.-
830 M.: Measurement of the nucleation of atmospheric aerosol particles, *Nat. Protoc.*, 7, 1651-1667,
831 doi: 10.1038/nprot.2012.091, 2012.

832 Lai, S., Hai, S., Gao, Y., Wang, Y., Sheng, L., Lupascu, A., Ding, A., Nie, W., Qi, X., Huang, X., Chi, X.,
833 Zhao, C., Zhao, B., Shrivastava, M., Fast, J. D., Yao, X., Gao, H.: The striking effect of vertical
834 mixing in the planetary boundary layer on new particle formation in the Yangtze River Delta,
835 *Sci. Total Environ.*, 829, 154607, doi: <https://doi.org/10.1016/j.scitotenv.2022.154607>, 2022.

836 Lee, S.-H., Gordon, H., Yu, H., Lehtipalo, K., Haley, R., Li, Y., Zhang, R.: New Particle Formation in the
837 Atmosphere: From Molecular Clusters to Global Climate, *J. Geophys. Res.*, 124, doi:
838 10.1029/2018JD029356, 2019.

839 Li, K., Zhu, Y., Gao, H., Yao, X.: A comparative study of cloud condensation nuclei measured between
840 non-heating and heating periods at a suburb site of Qingdao in the North China, *Atmospheric*
841 *Environ.*, 112, 40-53, doi: <https://doi.org/10.1016/j.atmosenv.2015.04.024>, 2015.

842 Li, M., Liu, H., Geng, G., Hong, C., Liu, F., Song, Y., Tong, D., Zheng, B., Cui, H., Man, H., Zhang, Q.,
843 He, K.: Anthropogenic emission inventories in China: a review, *Natl. Sci. Rev.*, 4, 834-866, doi:
844 10.1093/nsr/nwx150 %J National Science Review, 2017.

845 Li, X., Li, Y., Cai, R., Yan, C., Qiao, X., Guo, Y., Deng, C., Yin, R., Chen, Y., Li, Y., Yao, L., Sarnela, N.,
846 Zhang, Y., Petäjä, T., Bianchi, F., Liu, Y., Kulmala, M., Hao, J., Smith, J. N., Jiang, J.:
847 Insufficient Condensable Organic Vapors Lead to Slow Growth of New Particles in an Urban
848 Environment, *Environ. Sci. Technol.*, 56, 9936-9946, doi: 10.1021/acs.est.2c01566, 2022.

849 Liu, H. J., Zhao, C. S., Nekat, B., Ma, N., Wiedensohler, A., van Pinxteren, D., Spindler, G., Müller, K.,
850 Herrmann, H.: Aerosol hygroscopicity derived from size-segregated chemical composition and
851 its parameterization in the North China Plain, *Atmos. Chem. Phys.*, 14, 2525-2539, doi:
852 10.5194/acp-14-2525-2014, 2014a.

853 Liu, M., Matsui, H.: Secondary Organic Aerosol Formation Regulates Cloud Condensation Nuclei in the
854 Global Remote Troposphere, *Geophys. Res. Lett.*, 49, e2022GL100543, doi:
855 <https://doi.org/10.1029/2022GL100543>, 2022.

856 Liu, X. H., Zhu, Y. J., Zheng, M., Gao, H. W., Yao, X. H.: Production and growth of new particles during
857 two cruise campaigns in the marginal seas of China, *Atmos. Chem. Phys.*, 14, 7941-7951, doi:
858 10.5194/acp-14-7941-2014, 2014b.

859 Lovejoy, E. R., Curtius, J., Froyd, K. D.: Atmospheric ion-induced nucleation of sulfuric acid and water,
860 *J. Geophys. Res. Atmos.*, 109, doi: <https://doi.org/10.1029/2003JD004460>, 2004.

861 Lu, H., Wang, G., Guo, H.: Ambient acidic ultrafine particles in different land-use areas in two
862 representative Chinese cities, *Sci. Total Environ.*, 830, 154774, doi:
863 <https://doi.org/10.1016/j.scitotenv.2022.154774>, 2022.

864 Lu, Y., Yan, C., Fu, Y., Chen, Y., Liu, Y., Yang, G., Wang, Y., Bianchi, F., Chu, B., Zhou, Y., Yin, R.,
865 Baalbaki, R., Garmash, O., Deng, C., Wang, W., Liu, Y., Petäjä, T., Kerminen, V. M., Jiang, J.,
866 Kulmala, M., Wang, L.: A proxy for atmospheric daytime gaseous sulfuric acid concentration
867 in urban Beijing, *Atmos. Chem. Phys.*, 19, 1971-1983, doi: 10.5194/acp-19-1971-2019, 2019.

868 Lupascu, A., Easter, R., Zaveri, R., Shrivastava, M., Pekour, M., Tomlinson, J., Yang, Q., Matsui, H.,
869 Hodzic, A., Zhang, Q., Fast, J. D.: Modeling particle nucleation and growth over northern
870 California during the 2010 CARES campaign, *Atmos. Chem. Phys.*, 15, 12283-12313, doi:
871 10.5194/acp-15-12283-2015, 2015.

872 Ma, N., Zhao, C., Tao, J., Wu, Z., Kecorius, S., Wang, Z., Groß, J., Liu, H., Bian, Y., Kuang, Y., Teich,
873 M., Spindler, G., Müller, K., van Pinxteren, D., Herrmann, H., Hu, M., Wiedensohler, A.:
874 Variation of CCN activity during new particle formation events in the North China Plain, *Atmos.*
875 *Chem. Phys.*, 16, 8593-8607, doi: 10.5194/acp-16-8593-2016, 2016.

876 Matsui, H., Koike, M., Kondo, Y., Takegawa, N., Wiedensohler, A., Fast, J. D., Zaveri, R. A.: Impact of
877 new particle formation on the concentrations of aerosols and cloud condensation nuclei around
878 Beijing, *J. Geophys. Res. Atmos.*, 116, doi: <https://doi.org/10.1029/2011JD016025>, 2011.

879 Matsui, H., Koike, M., Takegawa, N., Kondo, Y., Takami, A., Takamura, T., Yoon, S., Kim, S. W., Lim,
880 H. C., Fast, J. D.: Spatial and temporal variations of new particle formation in East Asia using
881 an NPF-explicit WRF-chem model: North-south contrast in new particle formation frequency,
882 *J. Geophys. Res. Atmos.*, 118, 11,647-611,663, doi: <https://doi.org/10.1002/jgrd.50821>, 2013.

883 Merikanto, J., Napari, I., Vehkamäki, H., Anttila, T., Kulmala, M.: New parameterization of sulfuric acid-
884 ammonia-water ternary nucleation rates at tropospheric conditions, *J. Geophys. Res. Atmos.*,
885 112, doi: <https://doi.org/10.1029/2006JD007977>, 2007.

886 Merikanto, J., Spracklen, D. V., Mann, G. W., Pickering, S. J., Carslaw, K. S.: Impact of nucleation on
887 global CCN, *Atmos. Chem. Phys.*, 9, 8601-8616, doi: 10.5194/acp-9-8601-2009, 2009.

888 Mikkonen, S., Romakkaniemi, S., Smith, J. N., Korhonen, H., Petäjä, T., Plass-Duelmer, C., Boy, M.,
889 McMurry, P. H., Lehtinen, K. E. J., Joutsensaari, J., Hamed, A., Mauldin Iii, R. L., Birmili, W.,
890 Spindler, G., Arnold, F., Kulmala, M., Laaksonen, A.: A statistical proxy for sulphuric acid
891 concentration, *Atmos. Chem. Phys.*, 11, 11319-11334, doi: 10.5194/acp-11-11319-2011, 2011.

892 Morrison, H., Thompson, G., Tatarskii, V.: Impact of Cloud Microphysics on the Development of Trailing
893 Stratiform Precipitation in a Simulated Squall Line: Comparison of One and Two-Moment
894 Schemes, *Mon Weather Rev*, 137, 991-1007, doi: 10.1175/2008MWR2556.1, 2009.

895 Nieminen, T., Kerminen, V. M., Petäjä, T., Aalto, P. P., Arshinov, M., Asmi, E., Baltensperger, U.,
896 Beddows, D. C. S., Beukes, J. P., Collins, D., Ding, A., Harrison, R. M., Henzing, B., Hooda,
897 R., Hu, M., Hörrak, U., Kivekäs, N., Komsaare, K., Krejci, R., Kristensson, A., Laakso, L.,
898 Laaksonen, A., Leaitch, W. R., Lihavainen, H., Mihalopoulos, N., Németh, Z., Nie, W., O'Dowd,
899 C., Salma, I., Sellegri, K., Svenningsson, B., Swietlicki, E., Tunved, P., Ulevicius, V., Vakkari,
900 V., Vana, M., Wiedensohler, A., Wu, Z., Virtanen, A., Kulmala, M.: Global analysis of
901 continental boundary layer new particle formation based on long-term measurements, *Atmos.*
902 *Chem. Phys.*, 18, 14737-14756, doi: 10.5194/acp-18-14737-2018, 2018.

903 Petäjä, T., Mauldin, I. R. L., Kosciuch, E., McGrath, J., Nieminen, T., Paasonen, P., Boy, M., Adamov,
904 A., Kotiaho, T., Kulmala, M.: Sulfuric acid and OH concentrations in a boreal forest site, *Atmos.*
905 *Chem. Phys.*, 9, 7435-7448, doi: 10.5194/acp-9-7435-2009, 2009.

906 Pierce, J., Riipinen, I., Kulmala, M., Ehn, M., Petäjä, T., Junninen, H., Worsnop, D., Donahue, N.:
907 Quantification of the volatility of secondary organic compounds in ultrafine particles during
908 nucleation events, *Atmos. Chem. Phys.*, 11, 14495-14539, doi: 10.5194/acpd-11-14495-2011,
909 2011.

910 Pöschl, U., Canagaratna, M., Jayne, J. T., Molina, L. T., Worsnop, D. R., Kolb, C. E., Molina, M. J.: Mass
911 Accommodation Coefficient of H₂SO₄ Vapor on Aqueous Sulfuric Acid Surfaces and Gaseous
912 Diffusion Coefficient of H₂SO₄ in N₂/H₂O, *J. Phys. Chem. A*, 102, 10082-10089, doi:
913 10.1021/jp982809s, 1998.

914 Qiao, X., Yan, C., Li, X., Guo, Y., Yin, R., Deng, C., Li, C., Nie, W., Wang, M., Cai, R., Huang, D., Wang,
915 Z., Yao, L., Worsnop, D. R., Bianchi, F., Liu, Y., Donahue, N. M., Kulmala, M., Jiang, J.:
916 Contribution of Atmospheric Oxygenated Organic Compounds to Particle Growth in an Urban
917 Environment, *Environ. Sci. Technol.*, 55, 13646-13656, doi: 10.1021/acs.est.1c02095, 2021.

918 Ren, J., Chen, L., Fan, T., Liu, J., Jiang, S., Zhang, F.: The NPF Effect on CCN Number Concentrations:
919 A Review and Re-Evaluation of Observations From 35 Sites Worldwide, *Geophys. Res. Lett.*,
920 48, e2021GL095190, doi: <https://doi.org/10.1029/2021GL095190>, 2021.

921 Riipinen, I., Sihto, S. L., Kulmala, M., Arnold, F., Dal Maso, M., Birmili, W., Saarnio, K., Teinilä, K.,
922 Kerminen, V. M., Laaksonen, A., Lehtinen, K. E. J.: Connections between atmospheric

923 sulphuric acid and new particle formation during QUEST III–IV campaigns in
 924 Heidelberg and Hyytiälä, *Atmos. Chem. Phys.*, 7, 1899-1914, doi: 10.5194/acp-7-1899-2007,
 925 2007.

926 Roldin, P., Swietlicki, E., Massling, A., Kristensson, A., Löndahl, J., Eriksson, A., Pagels, J., Gustafsson,
 927 S.: Aerosol ageing in an urban plume – implication for climate, *Atmos. Chem. Phys.*, 11, 5897-
 928 5915, doi: 10.5194/acp-11-5897-2011, 2011a.

929 Roldin, P., Swietlicki, E., Schurgers, G., Arneth, A., Lehtinen, K. E. J., Boy, M., Kulmala, M.:
 930 Development and evaluation of the aerosol dynamics and gas phase chemistry model ADCHEM,
 931 *Atmos. Chem. Phys.*, 11, 5867-5896, doi: 10.5194/acp-11-5867-2011, 2011b.

932 Saha, S., Moorthi, S., Wu, X., Wang, J., Nadiga, S., Tripp, P., Behringer, D., Hou, Y.-T., Chuang, H.-y.,
 933 Iredell, M., Ek, M., Meng, J., Yang, R., Mendez, M. P., van den Dool, H., Zhang, Q., Wang, W.,
 934 Chen, M., Becker, E.: The NCEP Climate Forecast System Version 2, *J. Clim.*, 27, 2185-2208,
 935 doi: 10.1175/JCLI-D-12-00823.1, 2014.

936 Shen, X., Sun, J., Zhang, X., Zhang, Y., Wang, Y., Tan, K., Wang, P., Zhang, L., Qi, X., Che, H., Zhang,
 937 Z., Zhong, J., Zhao, H., Ren, S.: Comparison of Submicron Particles at a Rural and an Urban
 938 Site in the North China Plain during the December 2016 Heavy Pollution Episodes, *J. Meteorol.*
 939 *Res.*, 32, 26-37, doi: 10.1007/s13351-018-7060-7, 2018.

940 Shrivastava, M., Fast, J., Easter, R., Gustafson, W., Zaveri, R., Jimenez, J., Saide, P., Hodzic, A.:
 941 Modeling organic aerosols in a megacity: comparison of simple and complex representations of
 942 the volatility basis set approach, *Atmos. Chem. Phys.*, 11, 6639-6662, doi: 10.5194/acpd-10-
 943 30205-2010, 2011.

944 Shrivastava, M. K., Lane, T. E., Donahue, N. M., Pandis, S. N., Robinson, A. L.: Effects of gas particle
 945 partitioning and aging of primary emissions on urban and regional organic aerosol
 946 concentrations, *J. Geophys. Res. Atmos.*, 113, doi: <https://doi.org/10.1029/2007JD009735>,
 947 2008.

948 Sihto, S. L., Kulmala, M., Kerminen, V. M., Dal Maso, M., Petäjä, T., Riipinen, I., Korhonen, H., Arnold,
 949 F., Janson, R., Boy, M., Laaksonen, A., Lehtinen, K. E. J.: Atmospheric sulphuric acid and
 950 aerosol formation: implications from atmospheric measurements for nucleation and early
 951 growth mechanisms, *Atmos. Chem. Phys.*, 6, 4079-4091, doi: 10.5194/acp-6-4079-2006, 2006.

952 Sihto, S. L., Mikkilä, J., Vanhanen, J., Ehn, M., Liao, L., Lehtipalo, K., Aalto, P. P., Duplissy, J., Petäjä,
 953 T., Kerminen, V. M., Boy, M., Kulmala, M.: Seasonal variation of CCN concentrations and
 954 aerosol activation properties in boreal forest, *Atmos. Chem. Phys.*, 11, 13269-13285, doi:
 955 10.5194/acp-11-13269-2011, 2011.

956 Tewari, M., Wang, W., Dudhia, J., LeMone, M. A., Mitchell, K., Ek, M., Gayno, G., Wegiel, J., Cuenca,
 957 R. 2016. Implementation and verification of the united NOAA land surface model in the WRF
 958 model [M].

959 Virtanen, A., Kannosto, J., Kuuluvainen, H., Arffman, A., Joutsensaari, J., Saukko, E., Hao, L., Yli-Pirilä,
 960 P., Tiitta, P., Holopainen, J. K., Keskinen, J., Worsnop, D. R., Smith, J. N., Laaksonen, A.:
 961 Bounce behavior of freshly nucleated biogenic secondary organic aerosol particles, *Atmos.*
 962 *Chem. Phys.*, 11, 8759-8766, doi: 10.5194/acp-11-8759-2011, 2011.

963 Wang, D.-W., Guo, H., Chan, C.: Diffusion Sampler for Measurement of Acidic Ultrafine Particles in the
 964 Atmosphere, *Aerosol Sci Technol*, 48, doi: 10.1080/02786826.2014.978937, 2014.

965 Wang, J., Li, M., Li, L., Zheng, R., Fan, X., Hong, Y., Xu, L., Chen, J., Hu, B.: Particle number size
 966 distribution and new particle formation in Xiamen, the coastal city of Southeast China in

967 wintertime, *Sci. Total Environ.*, 826, 154208, doi:
968 <https://doi.org/10.1016/j.scitotenv.2022.154208>, 2022.

969 Wang, Y., Wang, Y., Song, X., Shang, Y., Zhou, Y., Huang, X., Li, Z.: The impact of particulate pollution
970 control on aerosol hygroscopicity and CCN activity in North China, *Environ. Res. Lett.*, 18, doi:
971 10.1088/1748-9326/acde91, 2023.

972 Westervelt, D. M., Pierce, J. R., Riipinen, I., Trivitayanurak, W., Hamed, A., Kulmala, M., Laaksonen,
973 A., Decesari, S., Adams, P. J.: Formation and growth of nucleated particles into cloud
974 condensation nuclei: model–measurement comparison, *Atmos. Chem. Phys.*, 13, 7645-7663,
975 doi: 10.5194/acp-13-7645-2013, 2013.

976 Wu, H., Li, Z., Jiang, M., Liang, C., Zhang, D., Wu, T., Wang, Y., Cribb, M.: Contributions of traffic
977 emissions and new particle formation to the ultrafine particle size distribution in the megacity
978 of Beijing, *Atmospheric Environ.*, 262, 118652, doi:
979 <https://doi.org/10.1016/j.atmosenv.2021.118652>, 2021a.

980 Wu, L., Ling, Z., Shao, M., Liu, H., Lu, S., Zhou, S., Guo, J., Mao, J., Hang, J., Wang, X.: Roles of
981 Semivolatile/Intermediate-Volatility Organic Compounds on SOA Formation Over China
982 During a Pollution Episode: Sensitivity Analysis and Implications for Future Studies, *J.*
983 *Geophys. Res. Atmos.*, 126, e2020JD033999, doi: <https://doi.org/10.1029/2020JD033999>,
984 2021b.

985 Wu, Z., Hu, M., Yue, D., Wehner, B., Wiedensohler, A.: Evolution of particle number size distribution in
986 an urban atmosphere during episodes of heavy pollution and new particle formation, *Sci. China*
987 *Earth Sci.*, 54, 1772, doi: 10.1007/s11430-011-4227-9, 2011.

988 Yao, L., Garmash, O., Bianchi, F., Zheng, J., Yan, C., Kontkanen, J., Junninen, H., Mazon, S., Ehn, M.,
989 Paasonen, P., Sipilä, M., Wang, M., Wang, X., Xiao, S., Chen, H., Lu, Y., Zhang, B., Wang, D.,
990 Fu, Q., Wang, L.: Atmospheric new particle formation from sulfuric acid and amines in a
991 Chinese megacity, *Science*, 361, 278-281, doi: 10.1126/science.aao4839, 2018.

992 Yu, F.: Quasi-unary homogeneous nucleation of H₂SO₄-H₂O, *J. Chem. Phys.*, 122, 074501, doi:
993 10.1063/1.1850472, 2005.

994 Yu, F., Luo, G., Nair, A. A., Schwab, J. J., Sherman, J. P., Zhang, Y.: Wintertime new particle formation
995 and its contribution to cloud condensation nuclei in the Northeastern United States, *Atmos.*
996 *Chem. Phys.*, 20, 2591-2601, doi: 10.5194/acp-20-2591-2020, 2020.

997 Yu, F., Luo, G., Pryor, S. C., Pillai, P. R., Lee, S. H., Ortega, J., Schwab, J. J., Hallar, A. G., Leitch, W.
998 R., Aneja, V. P., Smith, J. N., Walker, J. T., Hogrefe, O., Demerjian, K. L.: Spring and summer
999 contrast in new particle formation over nine forest areas in North America, *Atmos. Chem. Phys.*,
1000 15, 13993-14003, doi: 10.5194/acp-15-13993-2015, 2015.

1001 Yuan, Q., Li, W., sz, Z., Yang, L., Chi, J., Sui, X., Wang, W.: Integrated evaluation of aerosols during
1002 haze-fog episodes at one regional background site in North China Plain, *Atmos Res*, 156, doi:
1003 10.1016/j.atmosres.2015.01.002, 2015.

1004 Yue, D. L., Hu, M., Zhang, R. Y., Wu, Z. J., Su, H., Wang, Z. B., Peng, J. F., He, L. Y., Huang, X. F.,
1005 Gong, Y. G., Wiedensohler, A.: Potential contribution of new particle formation to cloud
1006 condensation nuclei in Beijing, *Atmospheric Environ.*, 45, 6070-6077, doi:
1007 <https://doi.org/10.1016/j.atmosenv.2011.07.037>, 2011.

1008 Zaveri, R. A., Easter, R. C., Fast, J. D., Peters, L. K.: Model for Simulating Aerosol Interactions and
1009 Chemistry (MOSAIC), 113, doi: <https://doi.org/10.1029/2007JD008782>, 2008.

1010 Zaveri, R. A., Easter, R. C., Peters, L. K.: A computationally efficient Multicomponent Equilibrium
1011 Solver for Aerosols (MESA), *J. Geophys. Res. Atmos.*, 110, doi:
1012 <https://doi.org/10.1029/2004JD005618>, 2005.

1013 Zhang, Q., Jimenez, J. L., Canagaratna, M. R., Allan, J. D., Coe, H., Ulbrich, I., Alfarra, M. R., Takami,
1014 A., Middlebrook, A. M., Sun, Y. L., Dzepina, K., Dunlea, E., Docherty, K., DeCarlo, P. F.,
1015 Salcedo, D., Onasch, T., Jayne, J. T., Miyoshi, T., Shimojo, A., Hatakeyama, S., Takegawa, N.,
1016 Kondo, Y., Schneider, J., Drewnick, F., Borrmann, S., Weimer, S., Demerjian, K., Williams, P.,
1017 Bower, K., Bahreini, R., Cottrell, L., Griffin, R. J., Rautiainen, J., Sun, J. Y., Zhang, Y. M.,
1018 Worsnop, D. R.: Ubiquity and dominance of oxygenated species in organic aerosols in
1019 anthropogenically-influenced Northern Hemisphere midlatitudes, *Geophys. Res. Lett.*, 34, doi:
1020 <https://doi.org/10.1029/2007GL029979>, 2007.

1021 Zhao, B., Shrivastava, M., Donahue, N. M., Gordon, H., Schervish, M., Shilling, J. E., Zaveri, R. A.,
1022 Wang, J., Andreae, M. O., Zhao, C., Gaudet, B., Liu, Y., Fan, J., Fast, J. D.: High concentration
1023 of ultrafine particles in the Amazon free troposphere produced by organic new particle
1024 formation, *Proc. Natl. Acad. Sci. U.S.A.*, 117, 25344-25351, doi: doi:10.1073/pnas.2006716117,
1025 2020.

1026 Zhao, B., Wang, S., Donahue, N. M., Jathar, S. H., Huang, X., Wu, W., Hao, J., Robinson, A. L.:
1027 Quantifying the effect of organic aerosol aging and intermediate-volatility emissions on
1028 regional-scale aerosol pollution in China, *Sci. Rep.*, 6, 28815, doi: 10.1038/srep28815, 2016.

1029 Zheng, B., Tong, D., Li, M., Liu, F., Hong, C., Geng, G., Li, H., Li, X., Peng, L., Qi, J., Yan, L., Zhang,
1030 Y., Zhao, H., Zheng, Y., He, K., Zhang, Q.: Trends in China's anthropogenic emissions since
1031 2010 as the consequence of clean air actions, *Atmos. Chem. Phys.*, 18, 14095-14111, doi:
1032 10.5194/acp-18-14095-2018, 2018.

1033 Zhu, Y., Li, K., Shen, Y., Gao, Y., Liu, X., Yu, Y., Gao, H., Yao, X.: New particle formation in the marine
1034 atmosphere during seven cruise campaigns, *Atmos. Chem. Phys.*, 19, 89-113, doi: 10.5194/acp-
1035 19-89-2019, 2019.

1036 Zhu, Y., Sabaliauskas, K., Liu, X., Meng, H., Gao, H., Jeong, C.-H., Evans, G. J., Yao, X.: Comparative
1037 analysis of new particle formation events in less and severely polluted urban atmosphere,
1038 *Atmospheric Environ.*, 98, 655-664, doi: <https://doi.org/10.1016/j.atmosenv.2014.09.043>, 2014.

1039 Zhu, Y., Shen, Y., Li, K., Meng, H., Sun, Y., Yao, X., Gao, H., Xue, L., Wang, W.: Investigation of Particle
1040 Number Concentrations and New Particle Formation With Largely Reduced Air Pollutant
1041 Emissions at a Coastal Semi-Urban Site in Northern China, *J. Geophys. Res. Atmos.*, 126,
1042 e2021JD035419, doi: <https://doi.org/10.1029/2021JD035419>, 2021.

1043

1044